Method for interfacial energy determination of gold nanoparticles on solid surfaces

Mikaela Petersson

Faculty supervisors Prof. Knut Deppert and M.Sc. Sara Thorberg
Faculty opponent Assoc. Prof. Carina Fasth

A thesis presented for the degree of Master in Nanoscience
30 hp

LUND
UNIVERSITY

Solid State Physics
Lund University - Faculty of Engineering
Sweden

December 2019

Method for interfacial energy determination of gold nanoparticles on solid surfaces

Mikaela Petersson

Abstract

The high surface-to-volume ratio of nanoparticles (NPs) makes them an interesting source for scientific research. How interfacial energies interplay between such a small structure and a solid bulk surface, are important because of the versatile applications NPs regard.

In this thesis, a convenient and reliable method for interfacial energy determination was investigated. The interfacial energies were calculated using Young's equation, where the contact angle between particle and surface was determined using two different methods. Method 1 utilized imaging samples, tilted 85°, in SEM. Method 2 utilized height measurements using AFM, and width measurements from top-view imaging in SEM.

The NPs in this thesis were made of Au, and placed on Si wafers, on Al_2O_3 coated Si wafers, and on sapphire wafers. The Si samples were heated for 10 or 30 minutes at 600°C or for 3 minuter at 900°C. The Al_2O_3 coated Si and sapphire samples were heated at 800°C for 75 hours.

Regarding all substrates containing Si, the AuNPs became catalysts for nanowire (NW) growth and no energies could be calculated. This development was confirmed via TEM imaging on 60 nm AuNPs sintered for 30 min at 600°C. Using FFT of these particles, {1 1 1}- and {2 0 0}-planes were detected. These particles were concluded to be crystalline, but had no clear faceted shape.

The interfacial energies of AuNPs on sapphire wafers were determined for 30, 60 and 90 nm NPs to be 897.8 ± 176, 1295.8 ± 81.1 and 1546.4 ± 188.5 ergs/cm^2, respectively, by Method 1, and 1958.4 ± 144.3, 1883.4 ± 96.3 and 1830.8 ± 54.1 ergs/cm^2, respectively, by Method 2. The energies determined using Method 2 are closer to the value retrieved from literature, 1725 ergs/cm^2, which regard particles below 100 nm in diameter [1]. Due to lack of literature, the interfacial energies calculated in this thesis are only compared to R. M. Pilliar and J. Nutting, from 1967, and may not be the most recent nor accurate value.

Method 1 was determined to be a method strongly dependent on how well the SEM imaging was performed, and resulted in unreliable and unstable energies. Method 2 eliminated the human factor that Method 1 implied, but did not consider particle shape and unexpected changes that may occur. Method 1 was easier to use but Method 2 was settled to be the most reliable method resulting in more stable energy-values. However, Method 2 was unable to detect the unexpected change of NW growth. More research is needed to decide whether Method 2 can be applied in every-day research practice.

KEYWORDS: *Nanoparticles, sintering, interfacial energies, Young's equation, contact angle, Au, Si, silica, Sapphire, Al_2O_3, SEM, AFM, TEM, FFT*

Acknowledgements

First and foremost, I would like to express huge gratitude toward Sara Thorberg, who has guided me through the project and been a supportive, dedicated and patient supervisor during the laboratory sessions and the thesis writing. I wish her and her family well. Also thanks to Knut Deppert, who gave me the opportunity to write my masters thesis at Lund University at the department of Solid State Physics, and giving me feedback and guidance when needed.

I thank Peter Blomqvist at Lund University, and Peter Sondhauss and Andrius Jurgilaitis at MAX IV, for the hours helping me operating and imaging samples with AFM.

Thanks to Filip Lenrick for helping me generate a TEM lamella with FIB. Without Maria Messing I would not have been able to get TEM images. The help from Markus Snellman regarding fourier transform of the TEM images raised the level of my discussion in this thesis. Thanks to the aerosol group at Solid State Physics at Lund University for the valid discussions and feedback.

I am grateful for my friends for reading my thesis and coming with feedback and help. Lastly, I thank my family for being supportive, patient and loving, throughout my thesis work, and for their feedback, help and advice.

Super small versus super big!

How would super tiny particles, nanoparticles, interact with a material being a billion times larger? What energies come to play between such a small structure and such a big surface? Does this energy depend on the size of the nanoparticles? It is important to measure such change due to the various applications nanoparticles regard.

Nanoparticles are so small that one could fit about 10000 of them in a row to reach the width of a human hair. A particle that small will have a huge surface to volume ratio, and will therefore act and react differently compared to an everyday object. That makes nanoparticles very interesting to study, and they have several application areas, such as within medicine and electronics.

The energy between a nanoparticle and a big, "normal", surface, tells a story of how the two parts interact. When a surface with nanoparticles on it gets heated in an oven, the nanoparticles will interact with the surface. A great way of measuring this interaction is through the interfacial energies. It is important to understand this interaction and interfacial energies because it may help in the development of novel materials as well as semiconductor research, which is included in almost all electronics, including your mobile phone!

Heating nanoparticles on a surface will alter the energies between the nanoparticles and the surface on which they are situated. Therefore the shape of the nanoparticles will change, either stretching out to increase its contact area with the surface, so called wetting, or it will try to minimize it. Which of the shape changes that occurs partly depends on the composition of the particle and the surface.

In this thesis, energy and shape changes of nanoparticles on different surfaces were explored after heating them at different times and temperatures. As an example, the development of the nanoparticles shown in figure 1 was investigated. The particles are 30 nm in diameter and were heated at 600°C for 10 minutes. The difference in colour is due to differences in contrast and the images are taken on random particles. The particles were determined to be more round after heating them. This investigation was done to discuss how the interfacial energies develop between a super tiny particle and a super large surface when it is heated.

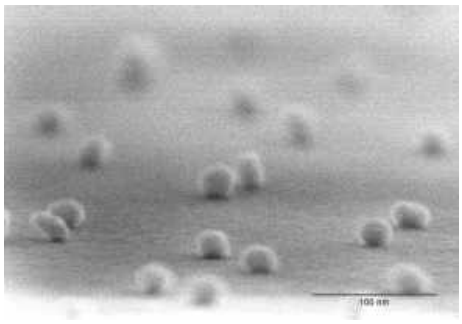

(a) Before heating.

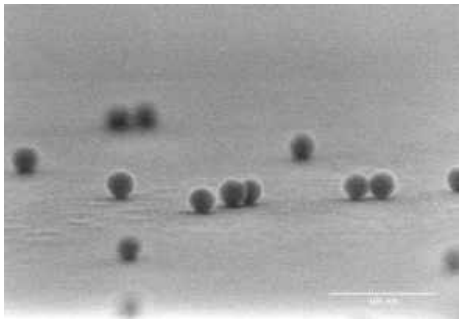

(b) After heating.

Figure 1: 30nm particles before and after heating at 600°C for 10 min.

Nomenclature

AFM Atomic Force Microscope

Al_2O_3 Aluminum oxide

ALD Atomic Layer Deposition

Au Gold

BCC Body Centered Cubic

DMA Differential Mobility Analyser

e/c evaporation/condensation

FCC Face Cenetered Cubic

FFT Fast Fourier Transform

FIB Focused Ion Beam

LOR Lift Off Resist

NP Nanoparticle

NW Nanowire

PdPt Palladium Platinum

RTP Rapid Thermal Processing

SEM Scanning Electron Microscope

Si Silicon

SPM Scanning Probe Microscopy

TEM Tunneling Electron Microscope

TMA Trimethylaluminum, $C_6H_{18}Al_2$

W Tungsten

Contents

List of Figures

List of Tables

Chapter 1

Introduction

Nanoparticles (NPs) are becoming a subject of increasing interest for scientific research, one reason being because of their versatile applications. Such applications include medical, such as for drug delivery [2] and cancer detection [3], as well as electronic, examples being sensors and probes [4].

The interest stems from the high surface-to-volume ratio when moving from bulk material toward the nanoscale, making NPs excellent for tasks such as catalysis and photocatalysis [5]. In short, NPs can be looked at as a bridge between atomic or molecular metric scales, and the bulk material scale. The large surface-to-volume ratio also results in changes in optical and electronic properties for the NPs [6].

Surface energies involving nanometer-sized structures are important for processes such as nucleation and growth of crystals and impact magnetic behaviour, crystal structure and chemical stability of materials [4]. To acquire deeper knowledge in regard to material science and material properties in the intermediate regime between single atoms and bulk material, research on interfacial energies regarding nanometer-sized objects on solid surfaces is important [7]. The interfacial energies between nanometer-sized objects and solid bulk surfaces will tell how materials interact, filling an important void in the scientific research world of solid state chemistry and solid state physics [8].

Increased knowledge of the interaction between NPs and solid surfaces, such as a metal/oxide systems, is also important due to the wide application areas of ceramics. Oxides are the most frequently used ceramics in many application areas, such as for catalysis [8, 9], making this research valuable.

1.1 Motivation of thesis

This thesis will provide deeper understanding of surface physics and chemistry of NPs on bulk material. The work will give insight into, and information on, how the different sizes within the nanometer size range will affect the interfacial surface energies.

Knowledge gained from the thesis work will clarify and help describe the bonding processes and the interfacial chemical reactions that take place between a nanometer sized object and a bulk material.

Results gained from the experiments will benefit scientific research within material science and allow for further bulk versus NP and atom scale research. This

will further the understanding of adhesion between materials, something which is of great importance in future research on nanostructures and the development of novel materials.

An efficient, fast and precise method for determining interfacial energies will simplify future research on the topic.

1.2 Aim of project

The main objective of this thesis was to determine the most suitable of two techniques for interfacial energy determination between NPs and solid surfaces. The determination was based on the criteria of reliability and ease of use. The interfacial energy determination was done using Young's equation, which required the contact angles between the NPs and substrate surface. These angles were determined using two different methods.

The first method involved Scanning Electron Microscopy (SEM) while tilting the samples, and the second utilized Atomic Force Microscopy (AFM) in combination with top-view imaging in SEM.

The two methods were used and compared using gold NPs (AuNPs) on Silicon (Si), Aluminumoxide (Al_2O_3), and sapphire surfaces. The AuNPs investigated had a diameter of 30, 60 or 90 nm.

Evaluation of a sample using Transmission Electron Microscopy (TEM) and Fast Fourier Transform (FFT) clarified the physical state of the NPs and the chemical interface between the NPs and the substrate.

1.3 Background

1.3.1 Interfacial energy determination - Young's equation

When NPs are placed on a solid surface, the particles are subjected to surface and interfacial energies as well as surface and interfacial tensions. These energies and tensions will change if the particles are heated and/or cooled [10]. Surface tensions and surface energies are numerically equal and are both energies, but have different units, being $\frac{\mathrm{J}}{\mathrm{m}}$ and $\frac{\mathrm{J}}{\mathrm{m}^2}$ respectively [11].

Suppose that AuNPs are placed on a Si substrate, and that the substrate is heated until melting of the AuNPs occurs. The surface energy of a liquid NP depends on the amount of intermolecular bonds that are disrupted when a surface is created [10]. This energy is incresing with decreasing particle size [12]. The interfacial energies are the energies involved between the liquid droplet and the substrate. The surface tension of the NPs is the cohesive force of the atoms at the surface of the particle that keeps it in a droplet form when in a liquid state. The interfacial tensions are a measure of adhesive forces between the liquid phase of one substance, in this case Au, and the solid of a substrate, such as Si. This interfacial tension is high on a hydrophobic surface and low on a hydrophilic surface [10].

Wetting is spreading of a liquid particle onto a substrate. A high wetting surface occurs when the surface energy is stronger than the surface tension. The contact angles will depend on the elemental combination of the NPs and substrates. Thus

the interaction between a liquid droplet and a surface results in a larger or smaller wetting surface [10].

When a NP is heated for a sufficient amount of time at a certain temperature, it is assumed to have reached an equilibrium state having a smooth spherical shape. When this liquid particle at equilibrium state is cooled down slow enough, the atoms in the NPs will have time to reach energetically favourable positions. This will result in crystalline particles with a faceted shape, for the particles in solid state.

Au, being a metal with an Face Centered Cubic (FCC) crystal structure, will have the faceted shape seen in figure 1.1 in a solid state equilibrium state [1]. The two heights, r_1 and r_2, are different from each other.

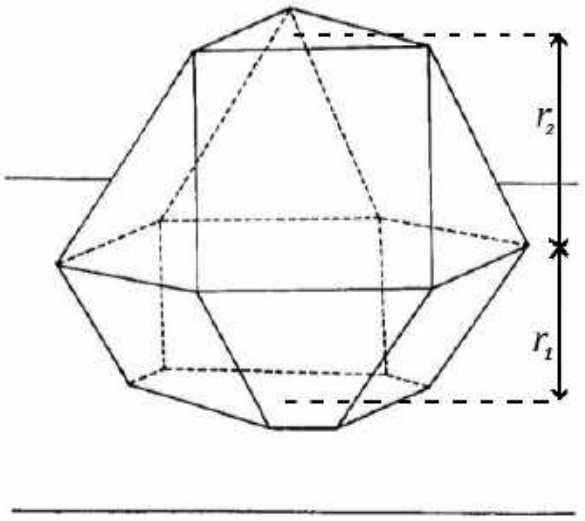

Figure 1.1: Schematic image of a AuNP in solid equilibrium state situated on a substrate surface, having an faceted shape, with two heights r_1 and r_2 [1].

To analyze the shape of an equilibrated solid crystalline particle on a surface in this way is equivalent to analyze a sessile droplet being situated on a solid surface without the gravitational effects [1], and therefore Young's equation can be utilized.

Young's equation, seen in equation 1.1, describes a three phase intersection, determined by a balance of surface tensions. The equation can be described as the basis for all fields of science involving capillary action and wetting [13].

In equation 1.1, γ_{sv} is the solid vapour free energy, γ_{sl} is the solid/liquid interfacial free energy and γ_{lv} represents the liquid vapour free energy. The angle ϑ is the contact angle between the solid and the liquid [14].

$$\gamma_{sv} = \gamma_{sl} + \gamma_{lv} \cdot \cos(\vartheta) \tag{1.1}$$

Figure 1.2 presents a schematic visualisation of Young's equation.

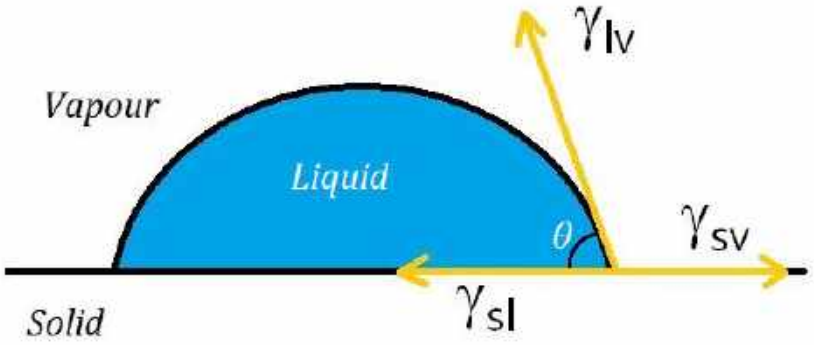

Figure 1.2: Schematic representation of a liquid droplet on a solid surface and the involved energies. γ_{sv} is the solid/vapour energy, γ_{sl} is the solid/liquid interfacial energy and γ_{lv} is the liquid/vapour energy. The contact angle is described as ϑ.

The contact angle of a droplet or particle measures the wettability of that particle on a surface. The lower the contact angle, the higher the surface energy, γ_{sv}, and interfacial tensions, and vice versa [10]. If $\vartheta < 90°$ the droplet is said to be hydrophilic and when ϑ moves closer to $0°$ the droplet is said to reach absolute wetting [15]. On the other hand, when $\vartheta > 90°$ the droplet is said to be hydrophobic, and when ϑ moves toward $180°$ there is no wetting of a liquid on a surface [15].

The constants γ_{lv} and γ_{sv} were taken from literature [1, 8, 16]. This way, γ_{sl} was extracted for the different particle sizes and sintering times, see equation 1.2.

$$\gamma_{sl} = \gamma_{sv} - \gamma_{lv} \cdot \cos(\vartheta) \tag{1.2}$$

During slow cooling, as opposed to quenching, the particles are presumed to have enough time to create an equilibrium shape in the solid form of the particles. Quenching is when you rapidly cool the material from a temperature which is above the recrystallization temperature but below the melting temperature, often done using water [17]. Quenching of the particles would result in the possible equilibrium droplet form being fixated.

In this thesis, the interfacial energies were determined using two different methods, utilising SEM as well as SEM and AFM respectively.

1. Method 1: The samples were put in a $90°$ sample holder and an added $5°$ tilt was added in the SEM. This resulted in the samples being tilted a total of $85°$ with respect to a horizontal axis. Measurements in the image were performed using the software ImageJ. The precision of this method depend on the quality of the SEM image.

    - In case of when the NPs had a faceted shape, r_1 and r_2 will be calculated using equation 1.3 and 1.4, visualised in the left image of figure 1.3. The interfacial energy is calculated using equation 1.5.

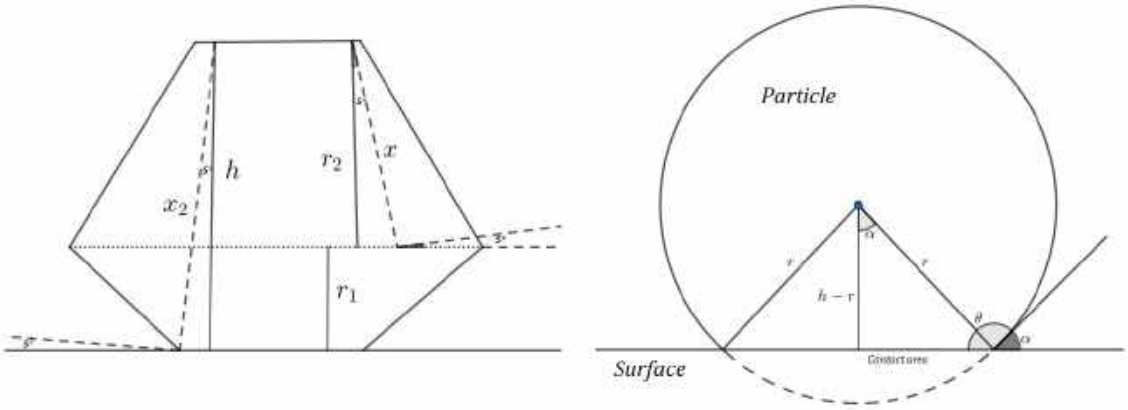

Figure 1.3: Visual representation of particles situated on a substrate surface and exposed to wetting. Approximation on how to calculate different dimensions of the particles with respect to the shape. If the particle is considered to have a round shape (right image), the 5° tilt is not considered as it would be for a faceted particle (right image). The length x and x_2, as well as r and h is measured via ImageJ. The droplet height is named as h. The shapes are related via $r_1 = h - r$ and $r_2 = r$ between the images.

The height r_1 is calculated using equation 1.3, where the value of r_2 is subtracted from the height h.

$$r_1 = h - r_2 = x_2 \cdot \cos(5^\circ) - x \cdot \cos(5^\circ) = \cos(5^\circ) \cdot (x_2 - x) \tag{1.3}$$

The height r_2 is calculated using equation 1.4

$$r_2 = x \cdot \cos(5^\circ) \tag{1.4}$$

The interfacial energy, using Young's equation, via the heights r_1 and r_2 is presented in equation 1.5. It is quite clear that the ratio of $\frac{r_1}{r_2}$ is a substitute to –cos(ϑ) in Young's equation.

$$\gamma_{sl} = \gamma_{sv} + \frac{r_1}{r_2} \cdot \gamma_{lv} \tag{1.5}$$

- If the NPs were spherical after sintering, the contact angle ϑ was measured directly using ImageJ. This is illustrated in figure 1.4.

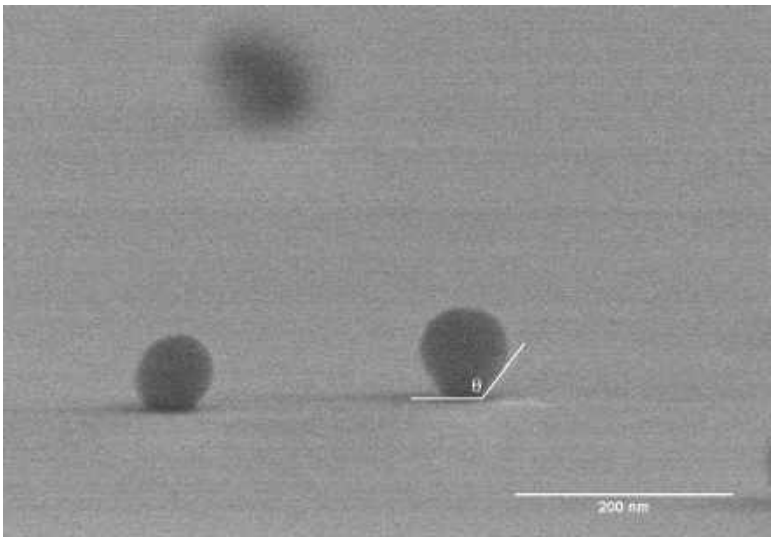

Figure 1.4: Illustration of how measurements of the contact angle was performed with ImageJ directly.

2. Method 2: Relied on height measurements from AFM together with diameter measurements from top view imaging in SEM. The process of extracting the contact angle ϑ in this method is referred to in the right image of figure 1.3 and equation 1.7. Note, however, that the calculated values of the contact angle require the particles to have a larger diameter than height, otherwise resulting in non-real values and the shape of the Au particle.

From figure 1.3 an expression for the angle ϑ is formed, see equation 1.6.

$$\cos(\vartheta) = \cos(180^\circ - \alpha) = \frac{h - r}{r} \tag{1.6}$$

Naturally, an expression of Young's equation is made as equation 1.7 suggests.

$$\gamma_{sl} = \gamma_{sv} + \frac{h - r}{r} \cdot \gamma_{lv} \tag{1.7}$$

During measurements, a number of random particles were measured upon for each sintering time/temperature. An average of the measured contact angles, heights and/or diameters, with a 95% confidence interval was determined to proceed with the interfacial energy calculations.

1.3.1.1 Solid/vapour and liquid/vapour energies

Relevant surface energies to determine γ_{sl} include γ_{lv} and γ_{sv}. The energy between the liquid, being gold, and vapour is described by equation 1.8. T_F describes the melting temperature of bulk gold, being T_F=1336K [8].

$$\gamma_{lv} = 1138 - 0.19 \cdot (T - T_F)[\mathrm{mJ/m^2 = ergs/cm^2}] \tag{1.8}$$

The temperature T describes a temperature that is relevant for the circumstances of the experiment.

Melting objects on the nanometer scale will require lower temperatures than bulk due to the large surface-to-volume ratio [18]. The small volume results in a

significant amount of diffusion during heating, even at the compaction temperature [19]. The compaction temperature is the temperature at which compaction from agglomerates into spherical particles occurs [20]. For further details, see Appendix A.1. The melting temperature of NPs, even when as small as 30 nm, is not far from the bulk melting temperature of 1336K, being approximately 900 °C [21]. On the other hand, the compaction temperature is clearly less for NPs with diameters ranging from 7-150 nm in diameter, and is 1/3 to 1/2 of the melting temperature [20]. This is motivation for the temperature T in equation 1.8 being set to 500°C, which is in between 1/3 and 1/2 of the melting temperature of Au. However, since the constant in front of the factor containing this temperature is the small number of 0.19, seen in equation 1.8, this temperature does not need to be too specific and the liquid-vapour energy, γ_{lv}, does not vary considerably from the chosen value of the temperature T.

With the temperature T in equation 1.8 being 500°C, or 773K, this results in a gold/vapour energy, γ_{lv}, of 1245 ergs/cm^2.

A drawback using equation 1.8 is that it describes the energy of mm sized droplets. In this thesis, this energy is, however, assumed possible to apply on the nm scales as well [8]. Also, it described the energy of liquid particles, and not for solid particles which is the goal of this thesis work [1, 16].

Regarding the Si substrate, the top layer will consist of a silicon oxide, SiO_x. This oxide will affect the relevant energies. In this thesis, the solid/vapour energy, γ_{sv}, was set to 275ergs/cm^2 [16].

Sapphire has the solid/vapour energy, γ_{sv}, of 995ergs/cm^2 [1].

1.3.2 Fast Fourier Transformation and crystal orientation

To discover any type of crystallographic orientation, and to examine the chemical development of sintered AuNPs, FFT manipulation was performed on TEM images of the particles.

Two concepts are important when considering FFT, real space and reciprocal space. Real space is where atoms are and crystals grow, and reciprocal space is a mathematical model constructed from a real space image. When using FFT of a crystal, you move from real space to reciprocal space. The reciprocal space can be used to understand crystal diffraction [22]. Figure 1.5 shows a schematic of FFT applied on a Body Centered Cubic (BCC) crystal, moving from real space to reciprocal space [23] .

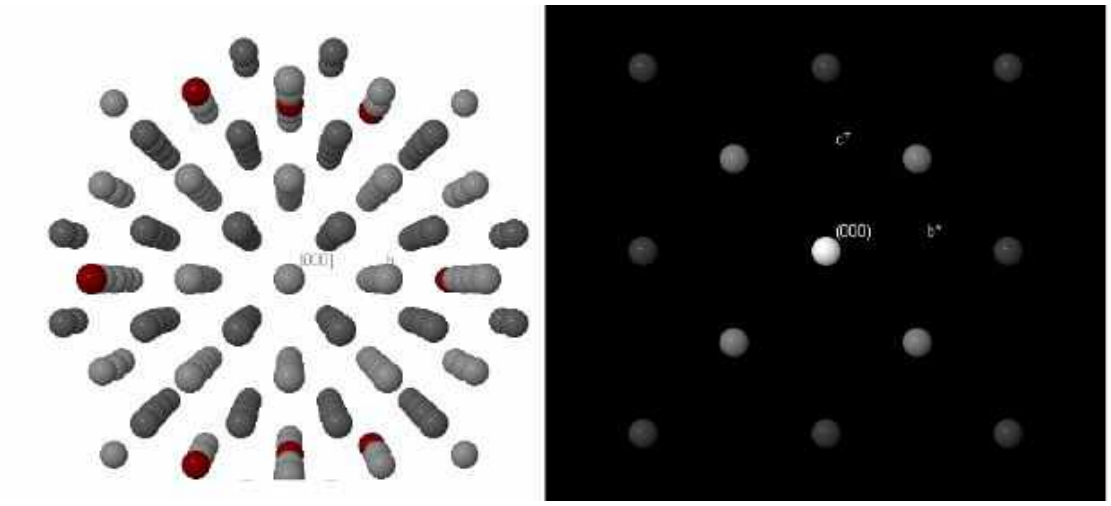

Figure 1.5: Schematic of BCC crystal in real space, left, and in reciprocal space, right. The center point marked (0 0 0) is from the electron beam. Taken from [23].

In the diffraction pattern in reciprocal space, one point represents one family of planes in real space. Therefore, the distance from the center point (0 0 0), see figure 1.5, to any other point in the diffraction pattern in reciprocal space, is related to interplanar distances in real space [22, 23]. The interplanar distance is the distance between two planes of a crystal.

The interplanar distance can be related to Miller indices, being a form of notation in crystals, and the lattice constant of the material, which is the size of the unit cell [24]. The interplanar distance, d_{hkl}, between two planes of a cubic crystal system is calculated using equation 1.9. In this equation, a_0 is the lattice constant and h, k and l are the Miller indices [24].

$$d_{hkl} = \frac{a_0}{\sqrt{h^2 + k^2 + l^2}} \tag{1.9}$$

For gold, the lattice constant a_0=4.065 Å [25]. To identify the planes of the particles detected via the FFT of the TEM images, the calculated interplanar distances and the interplanar distances retracted from FFT were compared. The four smallest interplanar distances of Au are presented in table 1.1.

Table 1.1: The smallest four interplanar distances of gold, with a_0=4.065 Å.

Miller indices (hkl)	**Interplanar distance d_{hkl} (Å)**
(1 0 0)	4.065
(1 1 0)	2.874
(1 1 1)	2.347
(2 0 0)	2.032

Miller indices can also be related to directions in a crystal. A crystallographic direction is a vector between two points in a unit cell or crystal, which passes through the origin of the coordinate system of the crystal. The Miller indices which describe crystallographic planes are denoted u, v, w, compared to when talking about planes which use the notations h, k, l [26]. The (1 0 0) plane and the [1 0 0] direction in a FCC unit cell is shown in figure 1.6.

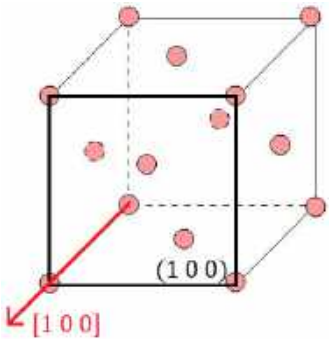

Figure 1.6: A FCC unit cell with the (1 0 0) plane and the [1 0 0] direction marked. Modified and taken from [27].

1.3.3 The experiments by R. M. Pilliar and J. Nutting

The experiments replicated in this thesis for the Au/Al_2O_3 system are presented and further described in the reference by R. M. Pilliar and J. Nutting (1967) [1]. The authors evaluated the interfacial energy of AuNPs on sapphire substrates, by observing the particles having a faceted shape but approximating them to be spherical, further utilizing a ratio of the two heights r_1 and r_2 as seen in figure 1.1. The two heights r_1 and r_2 were extracted from TEM images of the particles, which is quite time-consuming. The particles in the article were below 100 nm in diameter, which is a relevant size for comparison to results in this thesis, and were sintered at 1000°C for 75 hours. They found that the interfacial energy between the Au particles and the sapphire substrate, γ_{sl}, was 1725 ergs/cm^2, when using a solid/vapour energy, γ_{sv}, of 995 ergs/cm^2 [1].

Results presented in the article [1] are compared to results presented in this thesis for the Au/Al_2O_3 system. However, it is important to note that the article is quite old, and no updated values was found to compare with the results of this thesis.

Chapter 2

Methodology

AuNPs of different sizes were deposited on Si, Al_2O_3 coated Si, and sapphire wafers. The samples were sintered during different times and at different temperatures, and were then studied in SEM and AFM. In order to study the samples in TEM it is necessary to have very thin samples. One such thin sample was generated using a Focused Ion Beam (FIB). FFT of TEM images were performed.

Further, the interfacial energies between substrate and particle were determined by utilizing the two methods described. A more detailed description of the different steps of the methodology is described below as well as in Appendix A.

2.1 Particle production and sintering

The first step of this thesis work was to generate and deposit the particles on substrates. AuNPs with diameters of 30, 60 and 90 nm were generated and deposited using an evaporation/condensation (e/c) generator on Si wafers, Al_2O_3 coated Si wafers, and sapphire wafers. 50 nm of Al_2O_3 was deposited on Si using Atomic Layer Deposition (ALD). For further details about set-up and workings of the different methods practised, see Appendix A.

The AuNPs on Si wafers were sintered at 600°C for 10 and 30 min each, or at 900°C for 3 min, using a Rapid Thermal Processing furnace (RTP), RTP 1200-100.

The AuNPs on the Al_2O_3 coated Si wafers and the sapphire wafers were heated at 800°C for 75 hours. This is a lower temperature than used and presented in the referenced article [1], but due to limitations of the oven and for safety reasons, a lower temperature had to be used.

2.2 Generation of TEM lamella

A TEM sample was prepared to see the chemical and elemental interaction between particle and substrate. A FEI Nova Nanolab 600 FIB was used to cut a piece from a sample, (60 nm AuNPs on Si sintered for 30 min at 600°C), small enough for examination in a TEM. Due to lack of time, only one TEM lamella was generated.

2.2.1 Resist and PtPd deposition

Lift Off Resist (LOR) LOR0.7 was spin coated onto the sample to prevent residues from FIB milling to deposit onto the AuNPs, which otherwise could disturb TEM imaging.

Before deposition of the resist, the sample was cleaned using an ultrasonic bath of acetone followed by an ultrasonic bath of distilled water, for 20 s each. The sample was dried by baking for 5 min at 200°C.

The resist was deposited using 400 rpm during 5 s, followed by 1000 rpm during 45 s. The sample was baked on a hotplate at 200°C for 10 min. This resulted in a resist thickness of approximately 100 nm.

The deposited resist is soft and result in charging during SEM imaging. To avoid these disturbances, and to further protect the particles on the surface during TEM lamella generation, a protective layer was deposited over the resist. So, sputter-Q150T ES was used to deposit 10 nm Palladium Platinum (PdPt) on top of the LOR0.7. For further details about set-up and workings of the different methods applied, see Appendix A.

During the lamella generation, to protect the surface and the particles further, Tungsten (W) was deposited via the FIB.

The sapphire wafer samples were sputter coated with 4 nm PtPd before examination in SEM due to the non-conductive properties that sapphire possess.

2.3 Imaging and interfacial energy determination

The samples were studied in the SEM Hitachi SU8010 before sintering, and after every sintering time and temperature. The average particle diameter was determined using ImageJ of top-view images captured in SEM. The sample surface was examined using tapping mode in the Bruker AFM Icon in Lund Nano Lab and the Dimension 3100 Scanning Probe Microscope (SPM) at MAX IV. The software Gwyddion was used to determine the height of the particles from the AFM images. From the height and width, the contact angle was calculated geometrically. Young's equation, equation 1.1, was used to determine the interfacial energy of the particles.

Also, a vertical sample holder was used for the samples, see figure 2.1, together with a 5° tilt added in the microscope. The tilt was a compromise between as close to cross-sectional imaging as possible, and reasonable depth of field (the distance where the nearest and farthest object still are in focus). This made SEM imaging easier. The contact angles between substrate and particle was determined using ImageJ, and the interfacial energies were calculated using Young's equation, equation 1.1.

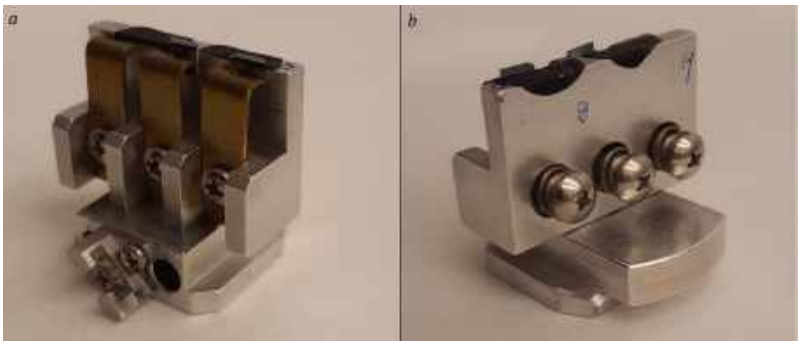

Figure 2.1: The vertical SEM sample holder with two samples from a) ahead and b) behind. The samples are clamped behind the three gold "teeth" seen in a).

The two ways of determining the interfacial energies were compared and discussed. The results were compared with literature and the most efficient way to determine interfacial energies on the nanometer scale was decided upon.

To get an understanding of the interfacial chemistry between the elements on the atomic level, TEM examination of a FIB generated lamella was performed using JEOL 3000F TEM at the National Center for High-resolution Electron Microscopy in Lund. FFT manipulation of the particles in the TEM images were performed to detect periodicity, crystal planes and crystal orientation. FFT and interplanar distance measurements were done using the software Gatans GMS, DigitalMicrograph.

Chapter 3

Results and Discussion

Regarding the choice of temperature, the compaction temperature for NP agglomerates is approximately 1/3 to 1/2 of the bulk melting temperature [20]. Therefore, the atoms in the NPs are estimated to have considerable movement at this temperature and the sintering temperature in this study will be chosen thereafter. In the case of Au, having the bulk melting temperature of 1064 °C [28], the temperature used for sintering of the Si wafers in the RTP was set to 600°C. Also a more drastic sintering temperature of 900°C was used for the RTP in hopes of some change occurring for the particles, if that would not have happened already. The sapphire and Al_2O_3 coated Si wafers were heated at 800°C in attempts of replicating the mentioned article [1].

All samples in this study were exposed to fast heating and slow cooling, as opposed to quenching. Quenching is rapid cooling of a material from above the recrystallisation temperature (between 150-200 °C for Au [29]) to room temperature by immersion in oil or water, and freezes the microstructure and stresses of the material [30]. Slow cooling results in longer periods for the atoms within the particles to find equilibrium positions in solid state. The slow cooling also avoids keeping alloying elements through diffusion [31] and residual stresses in the particles [32]. Therefore, slow cooling is preferred but not necessary for this thesis work, since both cases are accommodated for in the described methods used for interfacial energy determination.

As a reminder, Method 1 indicates the method where the samples were tilted 85° and imaged using SEM. If the particles were spherical the contact angel ϑ was measured, and if the particles had a faceted shape the height/radii were calculated. In both cases, ImageJ was utilized as a software tool to measure different parts of the particles. The calculation of ϑ using Method 2 uses height measurements from AFM imaging, and width determined from top-view SEM imaging.

One factor to consider is that no special surface treatment or cleaning of either substrate was performed before deposition of particles. Any dirt or local contamination would affect the energies of the particles of this area.

3.1 AuNPs on Si

The raw data of the height and diameters for the differently sized NPs, used for contact angle calculation of Method 2, is presented in Appendix B .The amounts of

particles that were measured on for the AuNPs being situated on Si for Method 1 and Method 2 is shown in Appendix B as well.

Representative images of the shape development of 30 nm AuNPs on Si substrates after different sintering times and temperatures are shown in figure 3.1. Particles such as seen in this image were used to measure the contact angle of Method 1.

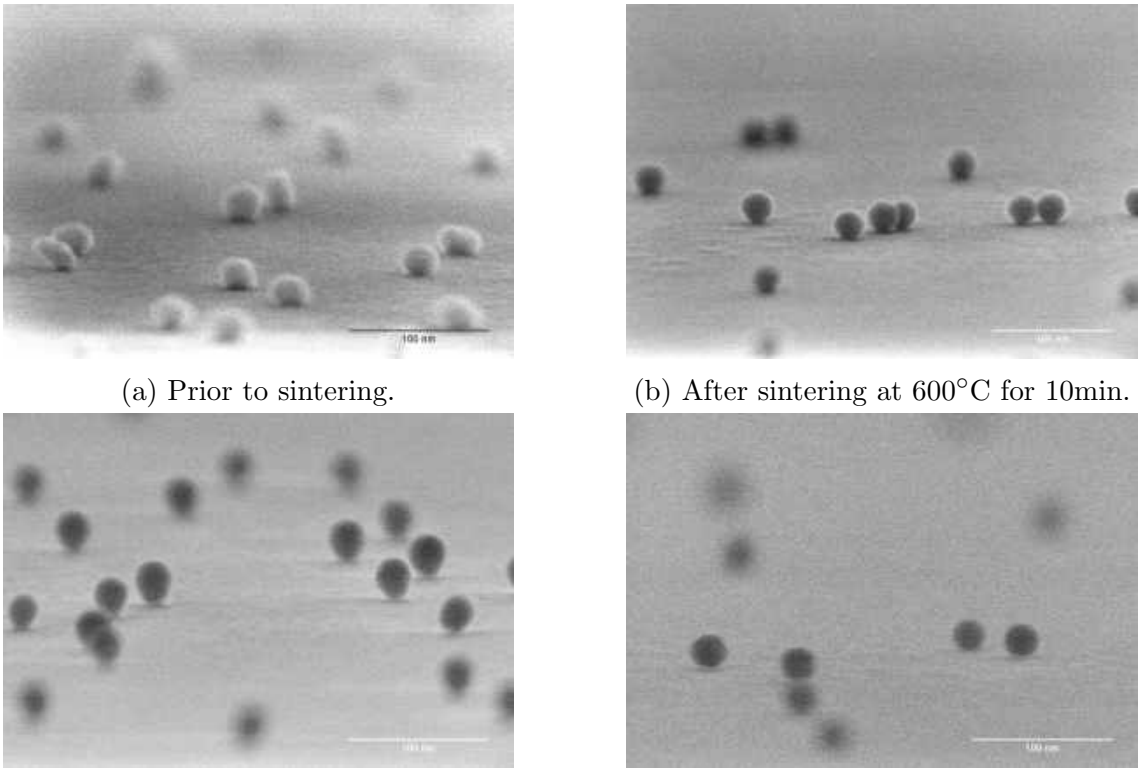

(a) Prior to sintering.

(b) After sintering at 600°C for 10min.

(c) After sintering at 600°C for 30min.

(d) After sintering at 900°C for 3min.

Figure 3.1: Changes of 30 nm AuNPs sintered at different times and temperatures.

With increasing sintering temperature the particles appear to become more spherical. This indicates some atomic movement/rearrangement, resulting in a AuNPs shape change even after 10 minutes of sintering. This can be seen in figure 3.1a and figure 3.1b. However, there is no sign of an equilibrium/faceted shape.

When the AuNPs have been sintered for 30 minutes at 600°C as well as for 3 minutes at 900°C the particles seem to be in no contact with the Si surface. This can be seen when observing figure 3.1c and figure 3.1d This change is assumed to be the cause of Vapour Liquid Solid (VLS) Si Nanowire (NW) formation, with the AuNPs functioning as catalysts for the process. During heating, Si atoms diffuse into the Au particle and then precipitate under the Au particle to create the NW during cooling. Further heating and higher temperatures would probably results in longer NWs [33]. The NW formation was not expected since no additional Si was introduced during the sintering process, which is typical for NW growth to occur [34]. Also, between the Si and the AuNPs there is a native oxide, which functions as a diffusion barrier, but apparently not that successfully. The results suggest that if NW formation has not yet occurred for the particles, it will when using the Au/Si elemental composition. Either with increasing temperature or sintering time, regardless of NP size in this thesis. This is something to consider for other

experiments where this elemental combination is used.

The elemental combination of Au/Si will be hard to use for interfacial energy determination, since the NPs eventually will not be in direct contact with the solid surface. Regardless, for the purpose of evaluating and compare Method 1 and Method 2 with respect to results, and to examine the development of the AuNPs on the Si surface when sintered, the contact angles were still measured. This would help in deciding which method one would rather use. The contact angles of 30 nm AuNPs on Si are presented in figure 3.2. The orange stacks describe the contact angles measured using Method 1, and the yellow stacks describe the contact angles derived using Method 2. The error bars indicate the 95% confidence interval of the values.

Since no faceted shape was detected, Method 1 only implies measuring the contact angle ϑ directly via ImageJ, without the need to calculate the values for any radii or heights.

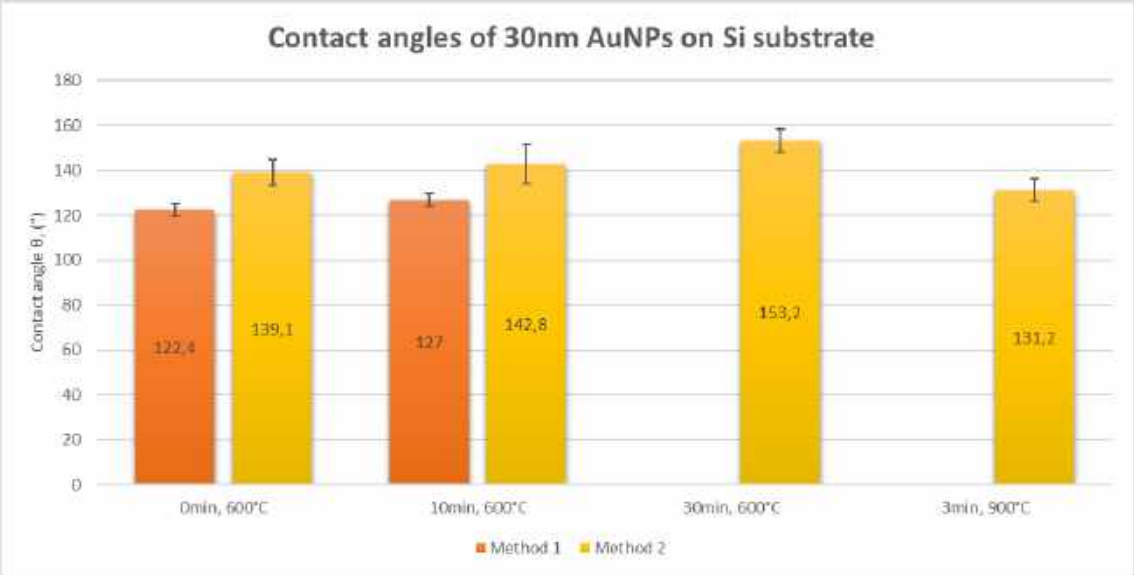

Figure 3.2: Contact angles, ϑ, of 30 nm AuNPs on Si substrates determined using Method 1 (orange stacks), and calculated using Method 2 (yellow stacks). The error bars mark the 95% confidence interval of the angles.

As seen in figure 3.2, the contact angles determined from Method 1 are missing for the samples being sintered for 30min at 600°C as well as when being sintered for 3 min at 900°C due to that the particles no longer being in direct contact with the surface. Method 2 did not register the NW formation, and therefore would yield an overestimation in heights. This would, in turn result in a higher value of the contact angle ϑ, which could be the case for the calculated contact angles seen in figure 3.2. Method 2 is blind to any unexpected changes that may occur between the substrate and the particles, which could discuss the method being flawed with regard to precision.

Method 1 seems to have a smaller margin of error compared to Method 2, but this could be because of a smaller sampling number when using AFM in Method 2. Also, since the error bars somewhat overlap within Method 1 and Method 2 respectively, there is no statistically reliable changes with regard to the contact angle development seen in figure 3.2.

The 60 and 90 nm AuNPs had no sign of a faceted shape. NW growth occurred for some of the 60 nm particles sintered for 3 minutes at 900°C but not for all. NW formation for 60 nm particles can be seen in figure 3.3. No NW formation was observed for the 90 nm particles. The shape development for the 60 nm and 90 nm AuNPs are presented in Appendix B. No new conclusions can be drawn from the contact angles of the 60 nm AuNPs, but are presented in Appendix B. When measuring the contact angles of the 60 nm AuNPs, no NW formation had occurred.

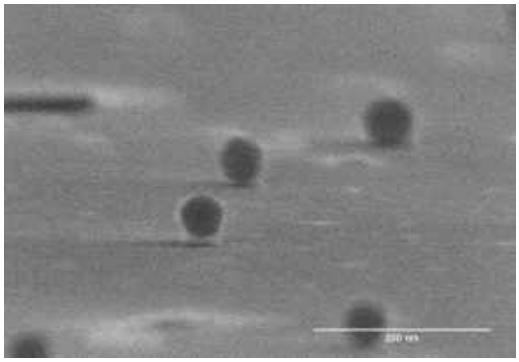

Figure 3.3: NW formation occurring for 60 nm AuNPs on Si surface after being sintered at 900°C for 3 minutes.

The contact angles for the 90 nm AuNPs can be seen in figure 3.4. There is roughly a 20° consistent difference of the contact angles between Method 1 (orange stacks), and Method 2 (yellow stacks). This could be due to difficulties during SEM imaging, or that the AFM could overestimate the heights of the particles. This would imply a systematic error when using the AFM, which would disturb the measurements.

Similar to the 30 and 60 nm particles, since no faceted shape was detected, Method 1 only entails measuring the contact angle ϑ directly.

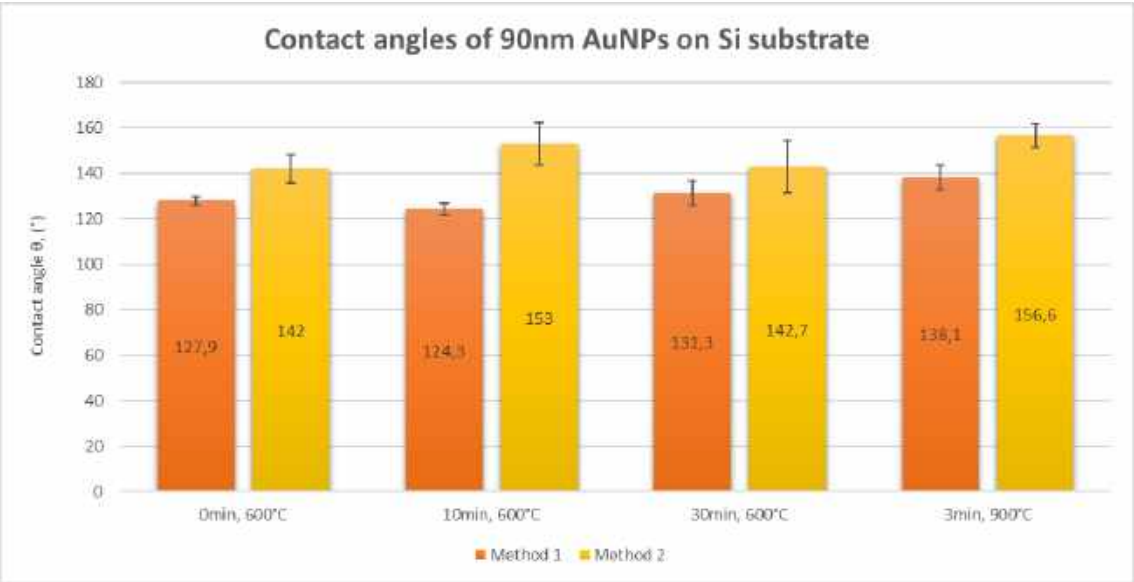

Figure 3.4: Contact angles, ϑ, of 90 nm AuNPs on Si substrates determined using Method 1 (orange stacks), and calculated using Method 2 (yellow stacks). The error bars mark the 95% confidence interval of the values.

If Method 1 and Method 2 is considered individually, again, there is no statistically reliable difference of ϑ over sintering time, nor with increasing temperature. This could indicate that neither method is sensitive enough to notice any shape changes of the particle, or that no noticeable change of the particles occur.

When comparing the contact angles between the particle sizes, there does not seem to be a severe difference. This suggests that the applied methods are not sensitive enough for varying particle sizes, or that the particle size-difference is not big enough for a difference between contact angles to occur.

3.1.1 TEM images and FFT manipulation

This section presents TEM images of 60 nm particles sintered at 600° for 30 min. FFT conversions of the TEM imaged particles are also presented.

A TEM image of the generated lamella is presented in figure 3.5. The different materials of the lamella are marked in the figure. The particles can be seen above the Si.

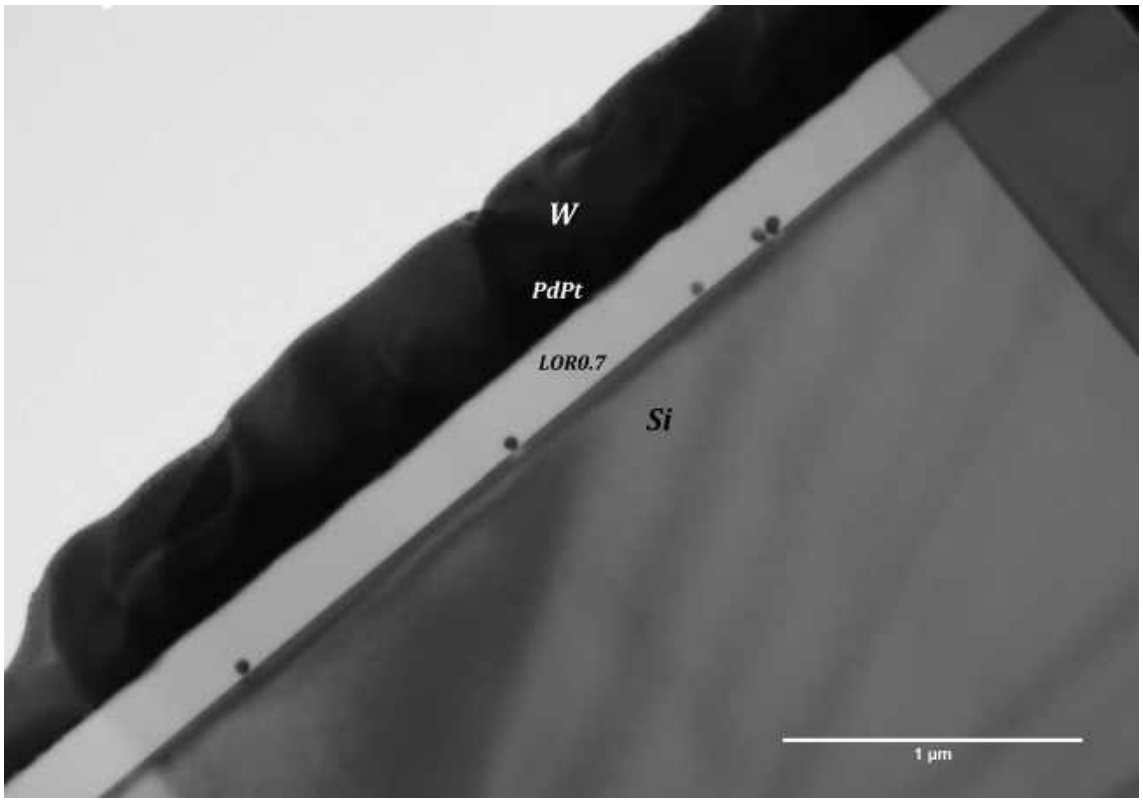

Figure 3.5: TEM image of the lamella with AuNPs on Si sintered at 600°C for 30 min. The different materials of the lamella are seen in the image (Si, LOR0.7, PdPt and W).

There are some structures seen within some of the particles. Figure 3.6 shows such structures, which are marked with yellow lines. This suggests that some orientation of the atoms occurred during the process of heating and cooling.

When examining the FFT of the particles, one can determine the interplanar distances by comparing the measured values from the particles, with the calculated values presented in Table 1.1. From FFT of the particle seen in figure 3.6, the interplanar distance was determined to be d = 2.22 Å. This value roughly corresponds to

the {1 1 1}-family of planes presented in Table 1.1. There seems to be several sets of spots pertaining to the {1 1 1}-family of planes. Also {2 0 0}-family of planes were detected in the particle, having a measured value of the interplanar distance equal to d = 1.98 Å. This analysis suggests several grains in the particle being randomly oriented.

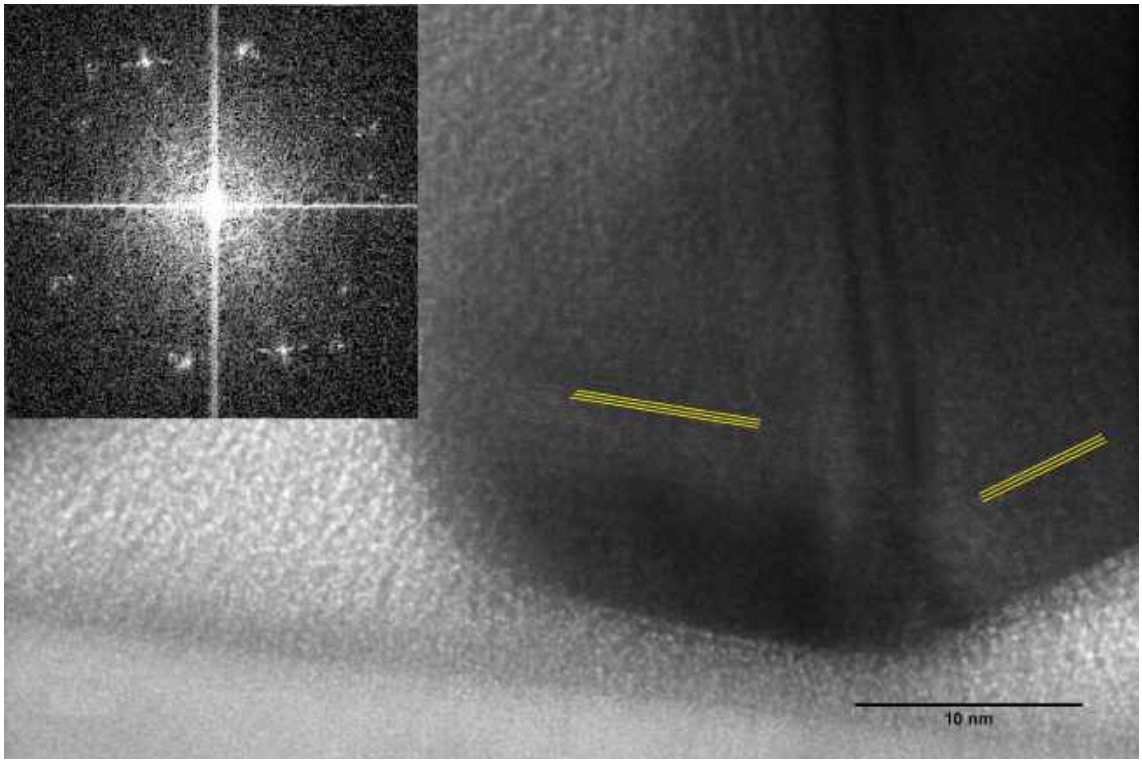

Figure 3.6: TEM image of part of an AuNP with the FFT seen in the top left corner. The FFT of the particle shows several sets of spots belonging to the {1 1 1}-family of planes, suggesting randomly oriented grains where the (1 1 1)-planes can be detected. There are some spots belonging to the {2 0 0}-family of planes as well.

The shadow below the particle in figure 3.6 suggest the beginning of NW formation.

Figure 3.7 shows an FCC unit cell with the (1 1 1) and (2 0 0) plane marked.

Figure 3.8 shows a NPs having another type of alignment with broader lines. The interplanar distance was determined to be d = 2.07 Å, being close to the interplanar distance corresponding to the {2 0 0}-family of planes presented in Table 1.1. The broad lines, corresponding to the spots marked with white circles in the FFT image of figure 3.8, are too broad to be the cause of one crystallographic orientation only. Therefore it could be several orientations interacting to create a new pattern. The resulting new pattern is called a Moiré pattern[35]. This suggests that different regions of the particle could have different orientations of the (2 0 0) planes.

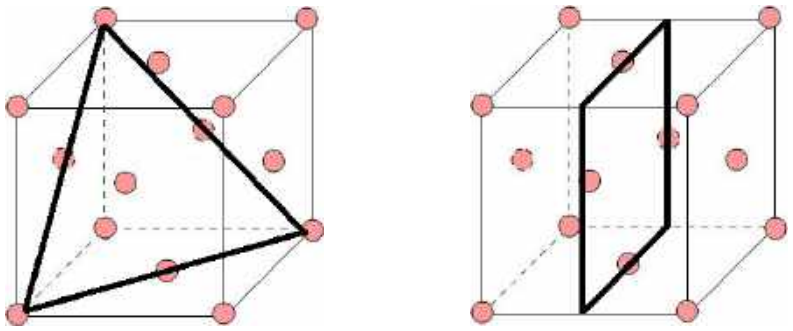

(a) (1 1 1) plane (b) (2 0 0) plane

Figure 3.7: FCC crystal structure with two different planes marked. Modified and taken from [27].

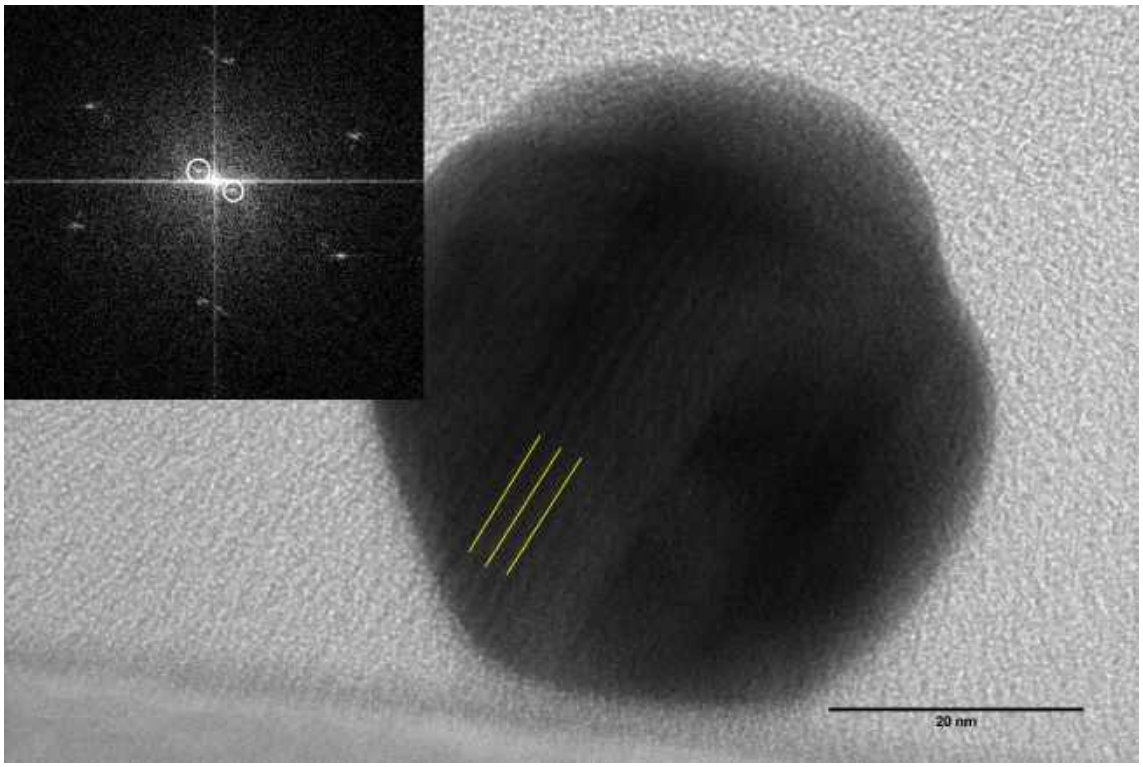

Figure 3.8: TEM image of a particle showing some indication of oriented atoms. The corresponding FFT is seen in the top left corner. The orientation across the particle, marked as yellow lines, seem too wide to be the result of simply one crystallographic orientation. This could be several orientations interacting, called a Moiré pattern. The spots in the FFT belonging to the Moiré pattern are marked using white circles. The FFT detected (2 0 0)-planes in the particle.

A similar shadow is seen below the particle in figure 3.8, as for the particle in figure 3.6. Again, this seems to be a beginning of NW formation. A schematic of a Moiré pattern is shown in figure 3.9.

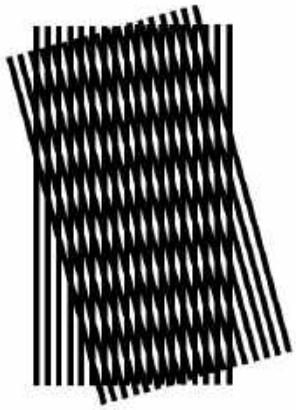

Figure 3.9: Illustration of a Moiré pattern, showing two identical patterns with different orientation create a third having a lower frequency.

Another TEM image together with the corresponding FFT for an AuNP is shown in figure 3.10. The FFT shows one set of spots, marked with white circles in the FFT. The spots in the FFT have low intensity. This could be due to the LOR0.7 resist being situated between the particle and the detector. This particle is determined to be crystalline, however, without having a faceted shape. The interplanar distance was determined using the FFT to be approximately d = 2.38 Å, again corresponding to (1 1 1)-plane accoring to Table 1.1.

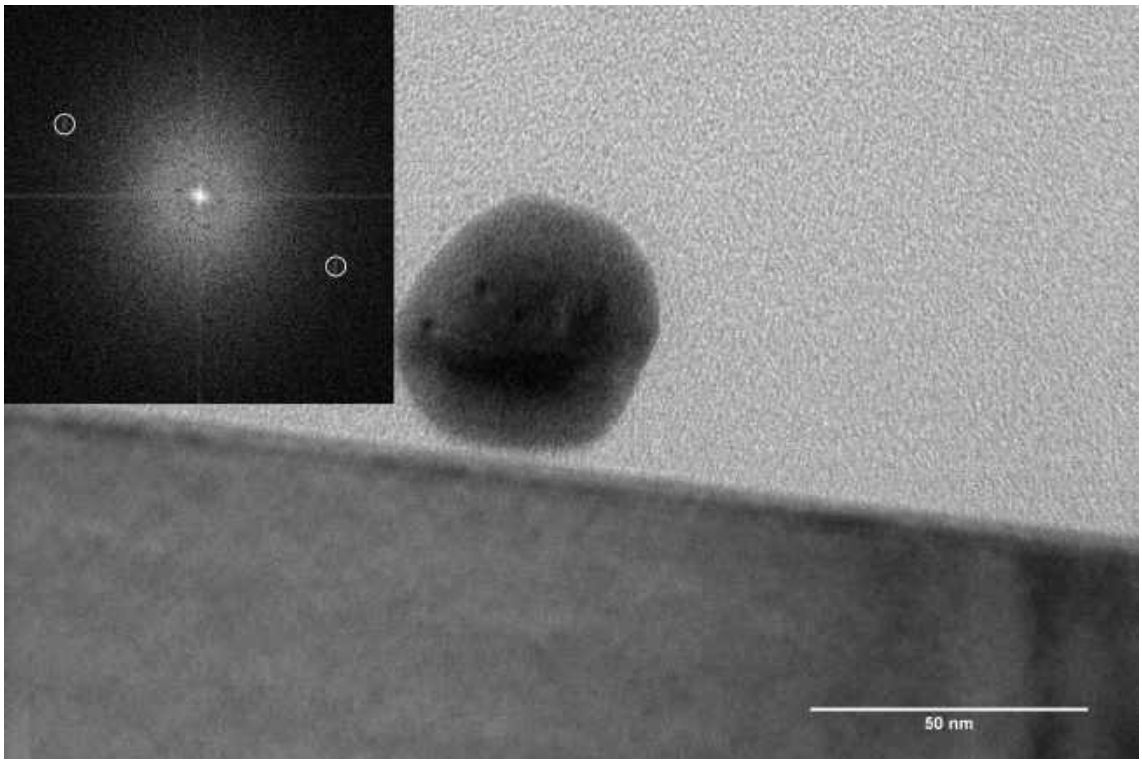

Figure 3.10: TEM image of an AuNP with the FFT seen in the top left corner. The particles does not show any sign of a faceted shape, but points in the FFT, marked with white circles, indicate some crystal orientation. (1 1 1)-planes in the particle were detected, having a single orientation throughout the crystal.

The particle in figure 3.10 seems to be floating and there is a slight contrast dif-

ference between the particle and substrate, but is again, probably the NW formation occurring.

Overall, the particles are concluded to be crystalline using TEM and FFT, but there are few signs of a faceted shape. This suggests that making conclusions on whether of not the particles have a faceted shape and/or are crystalline very difficult if one were only to use a SEM. In the article by R. M. Pilliar and J. Nutting, the particles shows a faceted shape being easier to distinguish [1]. On of these particles are shown in figure 3.11.

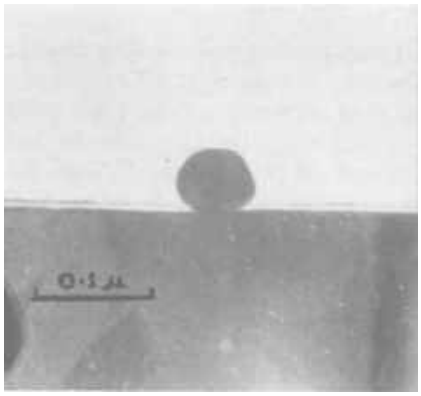

Figure 3.11: TEM image of AuNPs on a sapphire substrate taken from the article by R. M. Pilliar and J. Nutting [1]. The particle shows relatively clear sign of a faceted shape.

The particles in the article, however, were exposed to higher temperatures and longer sintering times compared to the Si samples in this thesis [1]. This suggests that the experiments in this thesis had too short sintering times and too low temperature. It is important to remember that the only sample used for TEM imaging was 60 nm AuNPs on Si, sintered for 30 min at 600°C. This means that the 30 nm AuNPs may have reached a faceted shape. More TEM imaging is needed for all samples.

3.2 AuNPs on Al_2O_3 coated Si

With regard to the samples heated for a longer time, the evaporation of Au from the particle can be quite palpable. But the diffusion of Si to the AuNPs could make noticeable change quite difficult to confirm.

The Al_2O_3 coated Si samples and sapphire samples were heated at 800°C for 75 hours, as presented in [1]. There was some indication suggesting the AuNPs had reached a solid/faceted equilibrium shape when heated during these circumstances. Figure 3.12a shows such indication with the particles having a hexagon-like shape when observed from above.

The elemental combination of Al_2O_3/Si still resulted in the formation of NWs. Figure 3.12b shows an example of such NW formation. Regardless of particle size NW formation occurred. Figure 3.12a demonstrates how cracks appeared below the particles making it possible for Si to diffuse to the AuNPs. The cracks can be due to tensions at the surface, which may be because of thermal expansion during the

sintering process, and the NPs placements above the cracks could be due to the particles having diffused there.

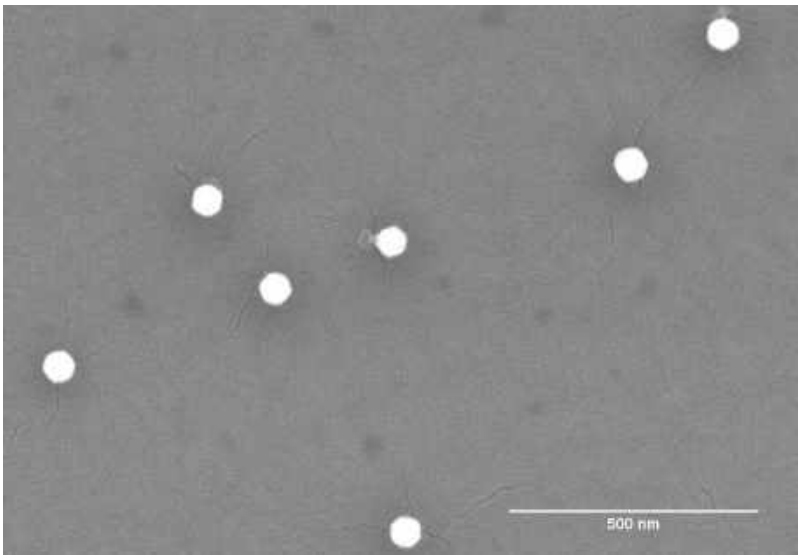

(a) From above.

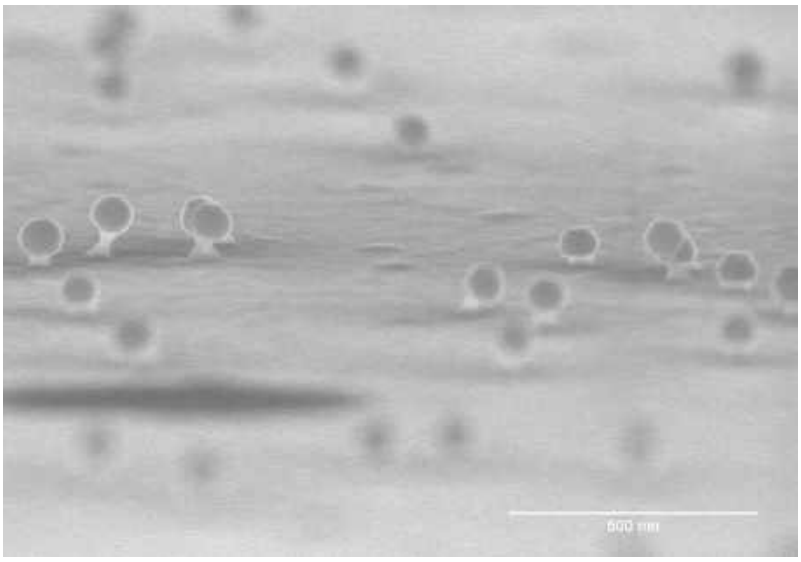

(b) With 85° tilt.

Figure 3.12: SEM images of 90 nm particles on Al_2O_3 sputtered on a Si wafer. The samples have been sintered at 800°C for 75 hours.

The samples where NW growth occurred were of no use for interfacial energy determination and were hence not be considered. The Au/Si and Au/Al_2O_3/Si elemental combinations are concluded to not be stable enough for this type of research.

3.3 AuNPs on sapphire

The heights and the diameters of the differently sized AuNPs situated on sapphire after sintering at 800°C for 75 hours, used for contact angle calculations of method 2, are presented in Appendix B. The number of particles that were used for measurements of Method 1 and Method 2 are also presented in Appendix B.

In the case of AuNPs on sapphire, no NW formation occurred. Figure 3.13 shows SEM images of the AuNPs before and after sintering at 800°C for 75 hours for the different particle sizes.

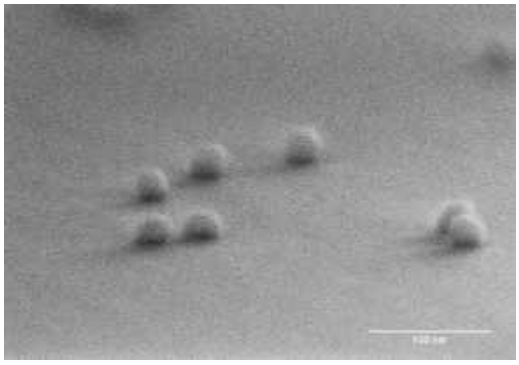

(a) 30 nm AuNPs prior to sintering.

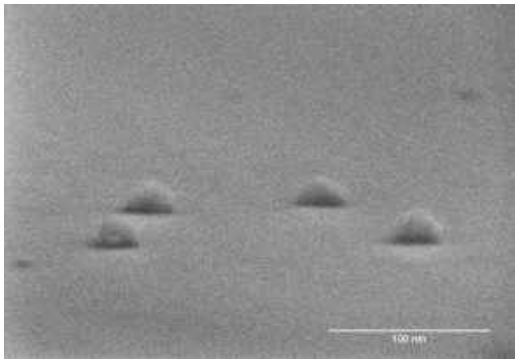

(b) 30 nm AuNPs after sintering.

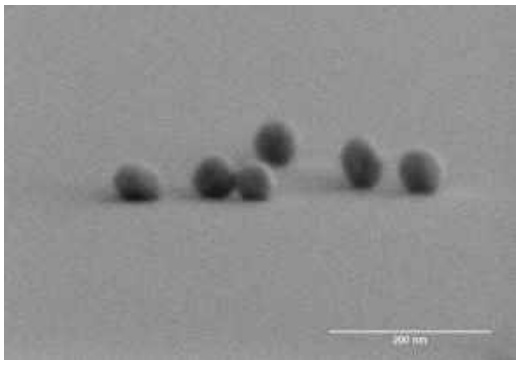

(c) 60 nm AuNPs prior to sintering.

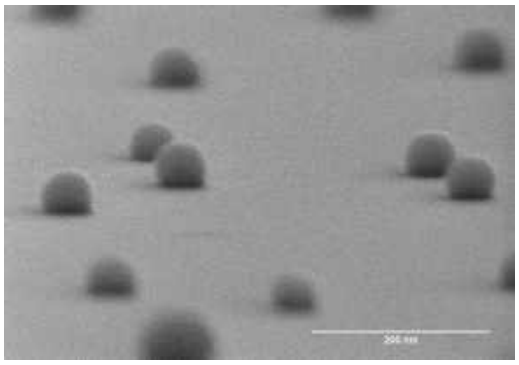

(d) 60 nm AuNPs after sintering.

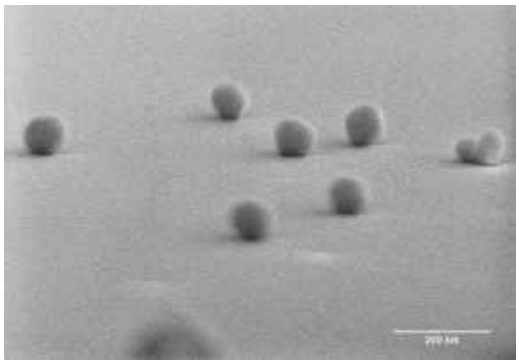

(e) 90 nm AuNPs prior to sintering.

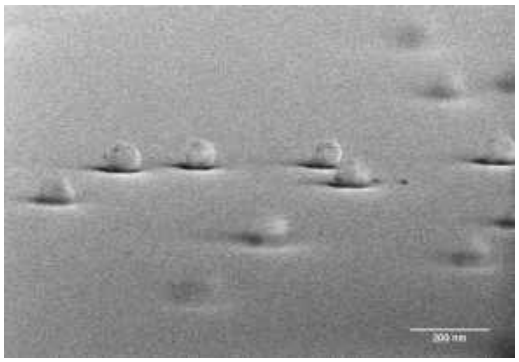

(f) 90 nm AuNPs after sintering.

Figure 3.13: Changes of differently sized AuNPs on sapphire substrates before and after sintering at 800°C for 75 hours. The samples are tilted 85° during imaging in SEM.

Figure 3.13b shows how the 30 nm AuNPs seem to have wetted to the surface after sintering. However, this type of wetting is not seen in the article by R. M. Pilliar and J. Nutting for roughly the same particle size and elements [1]. The wetted look of the particles can be due to astigmatism together with a slight defocus during SEM imaging. Charging of the sapphire samples makes imaging even more difficult, and a compromise was done between the amount of deposited PtPd and how clearly the contact angle would be measured in Method 1. Astigmatism of

the AuNPs/Si elemental combination was more easily accommodated for, due to no other disturbances being present (such as charging). From these statements, it is possible to judge Method 1 as being strongly dependent on perfect imaging in the SEM. Method 1 requires the focus to be perfect right at the particle-surface interface, which could become a problem due to the sensitive depth of field occurring at the tilt of 85°. To measure the height and width while tilting the samples 85° in SEM could be a possibility, but one has to consider the possible difficulties in imaging once again.

The SEM part of Method 2 includes, as described before, top-view imaging of the particles in SEM to extract the diameters. In the case of top-view imaging, the astigmatism and defocus is not as big of a problem and is more easily corrected for compared to when tilting the samples, as done in Method 1. This is because the depth of field is not as sensitive as it would be when tilting the samples.

Indication of the particles on sapphire in figure 3.13 reaching equilibrium shape is not as clear compared to when the AuNPs were situated on an Al_2O_3 coated Si surface. This may be because the changes of AuNPs on the sapphire wafers are much harder to detect due to charging during imaging.

The particles on the sapphire wafer will be treated as if no faceted shape occurred. However, a liquid equilibrium shape is estimated to have been reached during sintering. Cooling may have occurred too quickly, resulting in no faceted shape. To determine any faceted shape of the NPs using SEM might be inadequate. This determination might require TEM and FFT evaluation, which is a time consuming effort.

The statement that the particles may not have reached equilibrium shape could also be due to impurities during heating, affecting the particle shape development during sintering. This would suggest that the development of the particle to reach an equilibrium shape is less dependent of sintering time, and more of sintering conditions.

The collected and calculated contact angles of the different AuNPs sizes situated on sapphire is presented in figure 3.14.

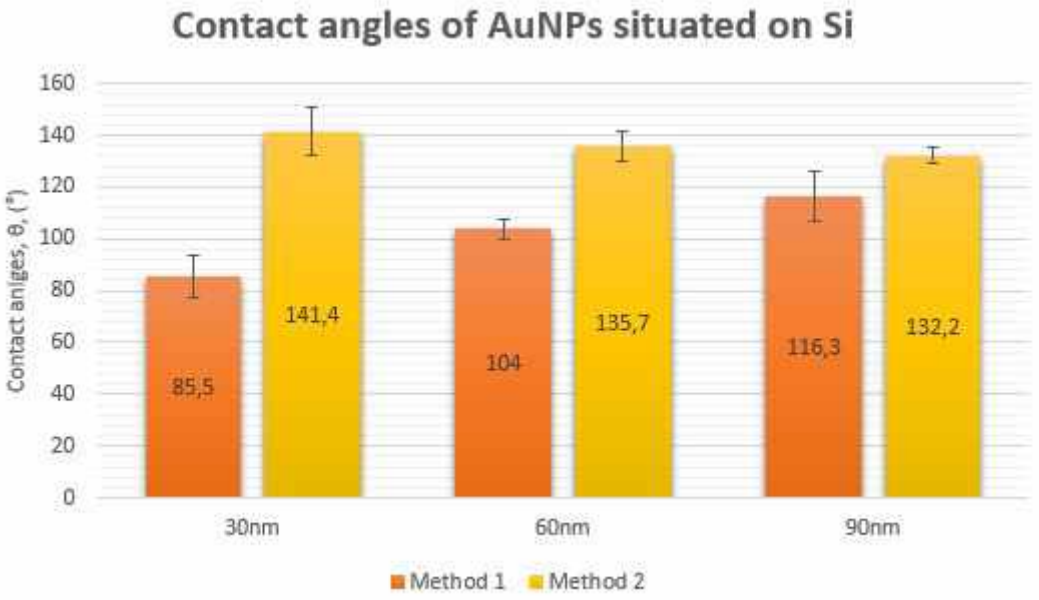

Figure 3.14: The contact angles ϑ collected using Method 1 and Method 2 on AuNPs situated on a sapphire surface, after sintering for 75 hours at 800°C.

The concluded interfacial energies of the AuNPs on a sapphire surface after being sintered at 75 hours at 800°C are shown in figure 3.15. However, when presenting the interfacial energies, a certain estimation has to be done that approximates the particles to be in some type of equilibrium state since residual stresses in the particles want to be avoided and could result in the particle relaxing even further after the sintering process.

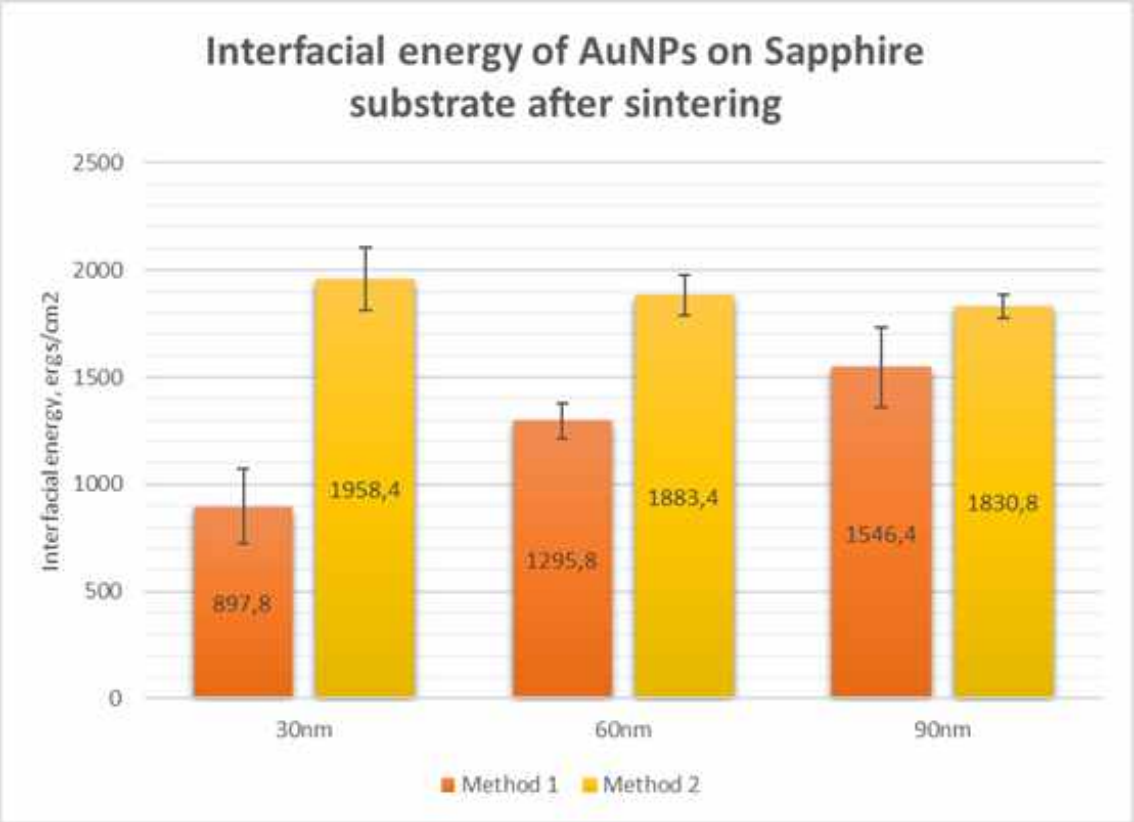

Figure 3.15: The interfacial energies in ergs/cm^2 of AuNPs on a Sapphire surface sintered at 800°C for 75 hours. The energies are calculated using ϑ derived from SEM, Method 1 (orange stacks), as well as SEM together with AFM, Method 2 (yellow stacks). The error bars mark the 95% confidence interval of the values.

As mentioned previously, the interfacial energy presented in the article by R. M. Pilliar and J. Nutting [1] was concluded to be 1725 ergs/cm^2, with no mention of specific particle size except for the particles being below approximately 100 nm in diameter. As seen in figure 3.15, this energy is not reached when using Method 1. Also, the energy drastically increases with particle size, making Method 1 much less reliable.

Even if the surface energy of the NPs increase with decreasing size, this should not affect the particles interfacial energy toward the bulk substrate too much which Method 1 seems to show. This argues for Method 2 being the more reliable and stable method with relation to the referenced article [1]. The energies extracted from Method 2 also resulted in reasonable size ranges, including the factor of 10^3 [16]. Considering the old nature of the article [1], and the overall lack of literature on the topic, an updated value of the interfacial energy between AuNPs and sapphire would be helpful in evaluating my methods.

3.4 The preferred method

Neither method is applicable when NW formation has begun, due to the particle leaving the surface and losing direct contact with the bulk. Also, Si may have diffused into the AuNPs and not have enough time to precipitate, changing the elemental composition of the particles.

Using Method 2 will result in a larger margin of error of the contact angles compared to Method 1. This could be a result of smaller sampling size from the AFM, compared to when measuring using only SEM. It would therefore be interesting to collect equal amounts of data for the two methods, making them more comparable. Method 1 is not a reliable method with regards to precision due to difficulties in distinguishing the contact angles as well as particle edges, if a faceted shape would be the case, during SEM imaging.

The gap between the contact angles when using the two methods can be from bias when measuring ϑ using Method 1. Also, the sample is tilted 5° from an ideal 90°, and is considered as if it were tilted 90°. This will affect the angle measurements done by ImageJ of Method 1. A larger part of human factors is depleted during calculation using Method 2, but requires the particle height to be smaller to, or equal to, the width of the particle. Also, to assure that no NW formation occurs, it will be necessary to examine the samples tilted in SEM regardless of the method used.

Method 1 implies difficult imaging, which argues for Method 2 being the more precise method for interfacial energy determination. One important factor to consider is that Method 2 is based on a series of estimations and approximations, and needs further experimental verification.

Chapter 4

Conclusions

The interfacial energy is only interesting if the NP has reached an equilibrium state. A faceted shape could not with certainty be detected during imaging in SEM for any particle size or shape. However, it could be that cooling of the samples after sintering occurred too quickly, or that impurities disturbed the equilibrium shape development. This would mean that the particles conserved the shape they acquired during sintering. TEM imaging with FFT of 60 nm AuNPs heated at 600°C for 30 min confirmed the particles to be crystalline, detecting (1 1 1)- and (2 0 0)- planes in the particles. Even though the particles were crystalline, they had no clear faceted shape. This would make any conclusions of crystalline particles difficult without using TEM and FFT. These methods are quite time consuming and several TEM lamellas would be needed to get a reasonable sampling size. So, if one would want the research to be based on statistical evaluations, this is not a very sustainable methods.

There is a consistent difference between the interfacial energies of AuNPs on sapphire wafers determined using the two different methods. The energies were determined for 30, 60 and 90 nm NPs to be 897.8 ± 176, 1295.8 ± 81.1 and 1546.4 ± 188.5 ergs/cm^2 respectively, by Method 1, and 1958.4 ± 144.3, 1883.4 ± 96.3 and 1830.8 ± 54.1 ergs/cm^2, respectively, by Method 2. The energies determined using Method 2 are closer to the value retrieved from literature, 1725ergs/cm^2 [1]. It is important to keep in mind that lack of literature makes comparisons very limited.

Method 1 is the most user-friendly method, but also a very uncertain one, resulting in unreliable and unstable contact angles and interfacial energies. These statements can be made due to difficulties in SEM imaging. Method 2 resulted in interfacial energies closer to literature, having a reasonable size range, and was settled to be the more reliable method. However, Method 2 was blind to any unexpected changes that might occur between the NPs and substrates, such as NW growth observed on several samples after sintering. This suggests that, when using Method 2, SEM study of the samples while tilting would be beneficial and a good compliment.

Further and more extended research on different types of elements is needed to confirm Method 2 to be a good method for interfacial energy determination. More TEM and composition analysis of the samples is required.

4.1 Outlook

To perform the experiments with a more controlled process of cooling of the samples would elevate the complexity of the experiments and the analysis. It would simplify which factors to consider in case the experiments of this thesis would be replicated.

Another factor to consider is some type of surface treatment before deposition of particles onto the substrates.

Overall, a wider spectrum of NP sizes, NP and substrate elements, sintering times, and sintering temperature would benefit the scientific approach of this thesis. Varying one factor at a time, keeping the others constant, would be interesting.

Studying specific NPs throughout cycles of heating at a certain, or several, temperatures would clarify the chemical and physical development between particle and substrate. This could be done via Environmental TEM or by marking/staining the different wafers and thereafter choosing particles to follow and study. Energy-dispersive x-ray Spectroscopy of TEM samples would help clarify the elemental partition throughout the particles to see if any diffusion between materials have occurred.

One factor to consider is to have equal amount of data collected for each method. This would make the methods even more comparable and the error bars would make clearer statements.

Summary

The aim of the project was to study the chemical interplay between a bulk material and NPs, and the interfacial energies this implies. Also, if there is a simple, fast and easy method to use for interfacial energy determination.

In this thesis, the contact angles and interfacial energies of AuNPs on solid surfaces are determined using Young's equation, where the contact angle ϑ was extracted using two different methods. Method 1 involved studying the samples in SEM while being tilted 85°. Method 2 utilized height measurements retrieved from AFM imaging, and width measurements from top-view imaging in SEM.

The particles were deposited on Si wafers, Al_2O_3 coated Si wafers and Sapphire wafers.

All samples substrates containing Si resulted in growth of NWs, with the AuNPs functioning as catalysts, suggesting that the Au/Si and Au/Al_2O_3/Si elemental combinations are unstable for this type of research. These samples could therefore not be used for interfacial energy determination. The AuNP interaction with the Si substrate through NW formation was confirmed via TEM imaging.

TEM in combination with FFT was used on one AuNPs/Si sample, and concluded crystalline particles. However, no faceted shape was detected regardless of particle size, sintering time nor sintering temperature.

When comparing Method 1 to Method 2, there is a consistent difference in contact angle between them. Method 2 resulted in higher, more stable values and energies closer to literature, compared to Method 1. With regards to one method or the other, there was no statistically reliable change in contact angle over sintering time for the AuNPs on the Si wafers (before NW growth occurred). This might suggest that either the methods are too insensitive to notice small changes, or that no changes of the particles occurred. Longer sintering times, higher sintering temperatures and/or slower cooling time might be a requirement to clearly notice change of particle shape, or for a faceted particle shape prevail.

Method 2 was determined to be a more reliable method due to the imaging difficulties and the unstable results of Method 1. The interfacial energies of AuNPs on sapphire wafers were determined for 30, 60 and 90 nm NPs to be 897.8 ± 176, 1295.8 ± 81.1 and 1546.4 ± 188.5 ergs/cm^2, respectively, by Method 1, and 1958.4 ± 144.3, 1883.4 ± 96.3 and 1830.8 ± 54.1 ergs/cm^2, respectively, by Method 2. The energies determined using Method 2 are closer to the value retrieved from literature, 1725 ergs/cm^2.

However, more research is needed to decide whether Method 2 method can be applied in every-day research practice.

Bibliography

[1] R. M. Pilliar & J. Nutting. "Solid-solid interfacial energy determinations in metal-ceramic systems". In: *The Philosophical Magazine: A Journal of Theoretical Experimental and Applied Physics* 16 (1967), p. 139.

[2] Hawk's Perch Technical Writing. *Nanotechnology in Medicine - Nanoparticles in Medicine*. 2019. Retrieved: Sept. 2019. URL: `https://www.understandingnano.com/medicine.html`.

[3] A. B. Chinen et al. "Nanoparticle Probes for the Detection of Cancer Biomarkers, Cells, and Tissues by Fluorescence". In: *Chem Rev* 19 (2015), p. 99.

[4] M. Bastiaan & H. Tjisse. "Size and shape dependency of the surface energy of metallic nanoparticles: unifying the atomic and thermodynamic approaches". In: *Physical Chemistry Chemical Physics* 20 (2018), p. 575.

[5] AZoNano. *The Applications & Suppliers of Nanoparticles*. 2016. Last updated 2019. Retrieved: Sept. 2019. URL: `https://www.azonano.com/article.aspx?ArticleID=4280`.

[6] J. Jeevanandam et al. "Review on nanoparticles and nanostructured materials: history, sources, toxicity and regulations." In: *Beilstein J Nanotechnol.* 9 (2018), p. 1050.

[7] T. Junno et al. "Contact mode atomic force microscopy imaging of nanometer-sized particles". In: *Applied Physics Letters* 66 (1995), p. 3295.

[8] N. Eustathopoulus. *Wettability at High Temperatures*. Ed. by M G. Nicolas & B. Drevet. Pergamon, 1999, p. 79.

[9] J. L. G. Fierro. *Metal Oxides: Chemistry and Applications 1st Edition*. Taylor & Francis group, 2013, p. 713.

[10] E. Y. Bormashenko. *Physics of Wetting: Phenomena and Applications of Fluids on Surfaces*. 2017.

[11] D. M. Mattox. *Handbook of Physical Vapor Deposition (PVD) Processing, 2nd edition*. William Andrew, 2010, p. 25.

[12] F. D Fischer & D. Beilstein D. Vollath. "Surface energy of nanoparticles – influence of particle size and structure". In: *Journal of Nanotechnology* 9 (2018), p. 2265.

[13] L. Makkonen. "Young's equation revisited". In: *Journal of Physics: Condensed Matter* 28 (2016), p. 5.

[14] M. Powers. *Principles for Understanding Heat Treating Materials: Brazing (Part 1)*. 2018. Retrieved: Sept. 2019. URL: https://www.californiabrazing.com/principles-understanding-heat-treating-materials-brazing-part-1/.

[15] J. T Simpson et al. "Superhydrophobic materials and coatings: A review". In: *Reports on progress in physics* 78 (2015), p. 3.

[16] D. L. Kantro & C. H. Weise S. Brunauer. "The surface energies of amorphous silica and hydrous amorphous silica". In: *Canadian Journal of Chemistry* 34 (1956), p. 1483.

[17] K.E.Lulay & D.J.Lloyd M.Taya. "Quenching of Metals Containing Impurity. I. Face-Centered-Cubic Metals". In: *Phys. Rev.* 148 (1966), p. 681.

[18] P. Antoniammal & D. Arivuoli. "Size and Shape Dependence on Melting Temperature of Gallium Nitride Nanoparticles". In: *Journal of Nanomaterials* 5 (2012), p. 22.

[19] F. Zhang et al. "Reduction of Plasmon Damping in Aluminum Nanoparticles with Rapid Thermal Annealing". In: *The Journal of Physical Chemistry C* 121 (2017), p. 56.

[20] M.N.A. Karlsson et al. "Compaction of agglomerates of aerosol nanoparticles: A compilation of experimental data". In: *Journal of Nanoparticle Research* 7 (2005), p. 43.

[21] F. Gao & Z. Gu. *Melting Temperature of Metallic Nanoparticles*. Ed. by M. Aliofkhazraei. Springer International Publishing, 2016, p. 661.

[22] M. Martínez-Ripoll. *Direct and Reciprocal lattices*. 1996. Updated: 2019. Retrieved: Nov. 2019. URL: http://www.xtal.iqfr.csic.es/Cristalografia/parte_04-en.html.

[23] K. D. Thelander. *Crystal Diffraction Patterns*. Lecture notes. 2017. Retrieved: Nov. 2019. URL: https://liveatlund.lu.se/departments/CAS/KASF15/KASF15_2017HT_100_1_NML__1281/CourseDocuments/KASF15.

[24] C. Deziel. *How to Calculate Interplanar Spacing*. 2019. Retrieved: Nov. 2019. URL: https://sciencing.com/calculate-interplanar-spacing-5628163.html.

[25] W. P. Davey. "Precision Measurements of the Lattice Constants of Twelve Common Metals". In: *Applied physic letters* 25 (1925), p. 753.

[26] M. Nespolo. "Direction indices for crystal lattices". In: *Journal of Applied Crystallography* 50 (2017), p. 1574.

[27] W. D.Callister. *Fundamentals of Materials Science and Engineering*. Ed. by D. G. Rethwinsch. John Wiley and Sons Ltd, 2008.

[28] G. Schmid & B. Corain. "Nanoparticulated Gold: Syntheses, Structures, Electronics, and Reactivities". In: *Journal of Inorganic Chemistry* 17 (2003), p. 3081.

[29] J.-H. Cho et al. "Recrystallization and Grain Growth of Cold drawn Gold bonding Wire". In: *Metallurgical and Materials Transactions A volume* 34 (2003), p. 117.

[30] B. L Bramfitt & A. O Benscoter. *Metallographer's Guide: Practices and Procedures for Irons and Steels*. ASM International, 2002, p. 284.

[31] A. P. Mouritz. *Introduction to Aerospace Materials*. Ed. by A. P. Mouritz. Woodhead publishing, 2012, p. 13.

[32] E. Troell et al. *Controlling the Cooling Process – Measurement, Analysis, and Quality Assurance*. Ed. by S. Hashmi et al. Elsevier, 2014, p. 99.

[33] Z. W. Pan et al. "Temperature-Controlled Growth of Silicon-Based Nanostructures by Thermal Evaporation of SiO Powders". In: *The Journal of Physical Chemistry B* 105 (2001), p. 2507.

[34] R. S. Wagner & W. C. Ellis. "Vapor-liquid-solid mechanism of single crystal growth". In: *Journal of Applied Physics* 4 (1964), p. 89.

[35] G. Oster & Y. Nishijima. "Moiré patterns". In: *Scientific American* 208 (1963), p. 54.

[36] H.G.Scheibel & J.Porstendörfer. "Generation of monodisperse Ag- and NaCl-aerosols with particle diameters between 2 and 300 nm". In: *Journal of aerosol science* 14 (1983), p. 126.

[37] J.I.T. Stenhouse & B.Y.H.Liu D.A. Japuntich. "An Aerosol Generator for High Concentrations of 0.5–5-m Solid Particles of Practical Monodispersity". In: *Aerosol Science and Technology* 16 (2007), p. 246.

[38] M. Messing. "Engineered Nanoparticles Generation, Characterization and Applications". PhD thesis. Lund University, 2011.

[39] L. S. Karlsson. "Transmission Electron Microscopy of III-V Nanowires and Nanotrees". PhD thesis. Lund University, 2007.

[40] P. Intra & N. Tippayawong. "An overview of differential mobility analyzers for size classification of nanometer-sized aerosol particles". In: *Songklanakarin Journal of Science and Technology* 30 (2008), p. 245.

[41] H. Holmgren. "On the Formation and Physical Behaviour of Exhaled Particles". PhD thesis. Chalmers university of technology, 2011.

[42] M.N.A Karlsson. "Methods to Generate Size- & Composition Controlled Aerosol Nanoparticles". PhD thesis. Lund University, 2004.

[43] MVSystems LLC - Thin Film Technologies. *Atomic Layer Deposition*. 2019. Retrieved: Sept. 2019. URL: http://www.mvsystemsinc.com/processes/atomic-layer-deposition/.

[44] D. Leadley. *Sputter deposition*. 2010. Retrieved: Aug. 2019. URL: https://warwick.ac.uk/fac/sci/physics/current/postgraduate/regs/mpagswarwick/ex5/growth/sd/.

[45] Chalmers university of technology. *Focused Ion-Beam (FIB)*. Published: 2015, Modified: 2017. Retrieved: Oct. 2019. URL: https://www.chalmers.se/en/researchinfrastructure/CMAL/instruments/FIB/FIB/Pages/default.aspx.

[46] S. Zaefferer & J. Konrad & D. Raabe. "Investigation of Orientation Gradients Around a Hard Laves Particle in a Warm-Rolled Fe_3Al-Based Alloy using a 3D EBSD-FIB Technique". In: *Acta Materialia* 54 (2006), p. 1369.

[47] J. Orloff & L. W. Swanson & M. Utlaut. "Fundamental limits to imaging resolution for focused ion beams". In: *Journal of Vacuum Science & Technology B* 14 (1996), p. 3759.

[48] Center for probing the nanoscale: An NSF Nanoscale Science and Engineering Center. *Scanning Probe Microscopy*. 2009. Retrieved: Oct. 2019. URL: https://teachers.stanford.edu/activities/SPMReference/SPMReference.pdf.

[49] J. Colvin. "(Opto)Electrical Characterization of III-V Semiconductor Nanowires Using SPM Techniques". Master thesis, Lund University. 2014.

[50] T. Junno et al. "Controlled manipulation of nanoparticles with an atomic force microscope". In: *Applied Physics Letters* 66 (1995), p. 3627.

[51] H.-Q Li & D. Thomas. *The Common AFM Modes*. 1997. Retrieved: Aug. 2019. URL: http://www.chembio.uoguelph.ca/educmat/chm729/afm/details.htm.

[52] M. Veerapandian & K. Yun. "Study of Atomic Force Microscopy in pharmaceutical and Biopharmaceutical Interactions - A Mini Review". In: *Current Pharmaceutical Analysis* 5 (2009), p. 256.

[53] D. Anderson. *What is a Limitation of Using Electron Microscopes to View Specimens?* 2017. Retrieved: Oct. 2019. URL: https://www.labx.com/resources/limitations-of-using-electron-microscopes-to-view-specimens/40.

[54] A. Nanakoudis. *SEM and TEM: what's the difference?* 2019. Retrieved: Sept. 2019. URL: https://blog.phenom-world.com/sem-tem-difference.

[55] I. Gutierrez-Urrutia & S. Zaefferer & D. Raabe. "Coupling of Electron Channeling with EBSD: Toward the Quantitative Characterization of Deformation Structures in the SEM". In: *Journal of The Minerals, Metals & Materials Society* 65 (2013), p. 1229.

[56] C. Celine. *Differences Between TEM and SEM*. 2012. Retrieved: Aug. 2019. URL: http://www.differencebetween.net/science/difference-between-tem-and-sem/.

Appendix A

Material deposition and microscopy techniques

A Material deposition

A.1 Particle generation and deposition

For this project, an aerosol method was used for generation of the differently sized NPs. The aerosol method used for generation and deposition of AuNPs was an e/c generator with a tandem Differential Mobility Analyzer (DMA) setup [36].

Using this type of e/c generator results in monodisperse aerosols with high specific size-selection and purity [37], desirable for the experiments executed in this thesis.

Figure A.1 describes a schematic of an e/c setup.

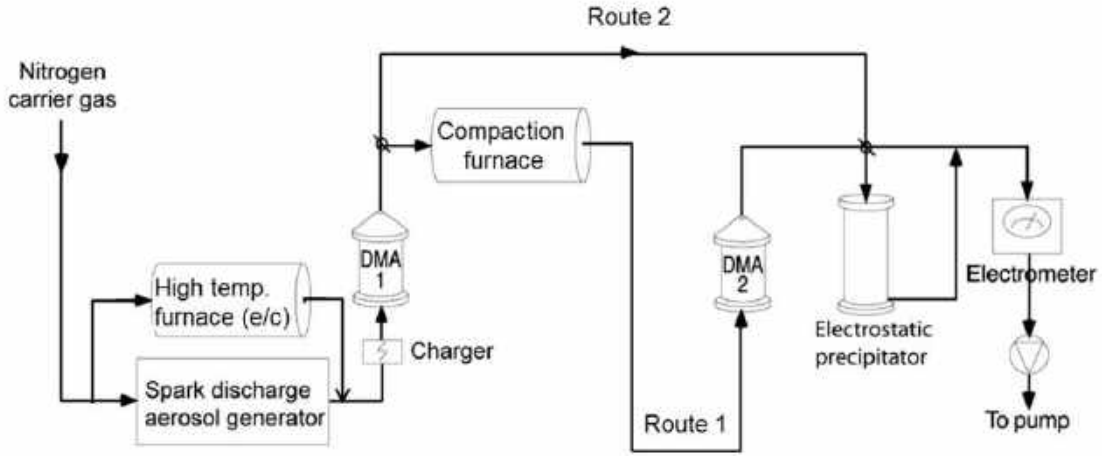

Figure A.1: Schematic of an e/c setup for NP production followed by deposition on a substrate through a pump. The DMAs select particles by size, and the two furnaces vaporize the metal and get spherical particles from agglomerates respectively. Taken from [38].

The generator operates by heating a solid piece of the desired element, in this case Au, to produce NPs. The Au is heated using a high temperature furnace until sufficient evaporation occurs. The generated vapor gas will be transported to cooler

regions in the furnace, where the gas will nucleate and create primary particles. These primary particles will generate agglomerates by collision. The agglomerates are carried away by a nitrogen gas. The agglomerates are charged and subsequently size-selected by a first DMA having a fixed voltage [39]. The workings of a DMA is described in figure A.2. More detailed description of the principle of a DMA can be found in P. Intra and N. Tippayawong [40].

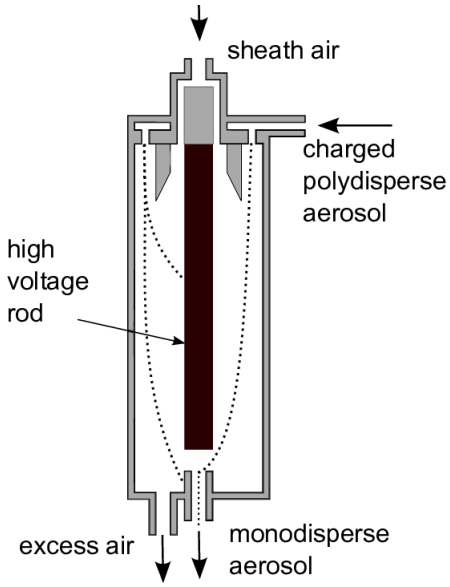

Figure A.2: Schematic representation of size-sorting of particles using a DMA with a set voltage [41]. A charged polydisperse aerosol gets sorted using a voltage rod in the DMA. This results in a monodisperse aerosol [38, 40] .

The size-selected agglomerates will then be exposed to a second furnace, a compaction furnace. This makes the agglomerates become spherical and crystalline particles by heating at a relevant compaction temperature. These particles are then subjected to a second size-sorting in a second DMA [42] (Route 1 in figure A.1) to generate particles with the desired size.

The electrostatic precipitator is used for controlled deposition of the generated particles onto a substrate. The charged particles will repel each other and avoid cluster-formation, thus the deposited particles will be well-dispersed on the substrate. The particles will be focused on the substrate surface using an electric field. An electrometer is used to measure the particle concentration [36, 37, 38].

A second size sorting, using the second DMA (Route 2 in figure A.1), is only necessary if a very specific particle size is desired [38].

Using a tandem-DMA set-up for the e/c generator, such as Route 1 in figure A.1, will result in a monodisperse aerosol with crystalline particles having a specific size, being well distributed on the substrate surface [36, 37, 38].

In this thesis, the temperature of the first furnace was set to 1800°C, 1825°C and 1875°C for each particle size, respectively. The temperature of the second furnace, the compaction temperature, was set to 600°C.

A.2 Atomic layer deposition

ALD is a cyclic precision deposition technique, enabling the possibility of nm thick layers with a high degree of conformity. ALD is an important technique for semiconductor and MEMS production. In this thesis, deposition of Al_2O_3 on a Si wafer was needed to create the AuNPs/Al_2O_3 elemental system.

Figure A.3 presents one cycle of Al_2O_3 deposition. The cycle uses water, H_2O, and trimethylaluminum, $C_6H_{18}Al_2$, (TMA) [43]. A hydroxylated surface, i.e. a surface having been exposed to water vapour, is exposed to TMA, figure A.3(a), where Al replaces the hydrogen atoms when reacting to the bound OH group, figure A.3(b). The remaining CH_3 groups will be carried away during the purge together with excess TMA. A pulse of H_2O, figure A.3(c), replaces the bound CH_3 group with OH, allowing for further attachment of Al during the following pulse of TMA after the purge removing the remaining H_2O and CH_4, figure A.3(d) [43].

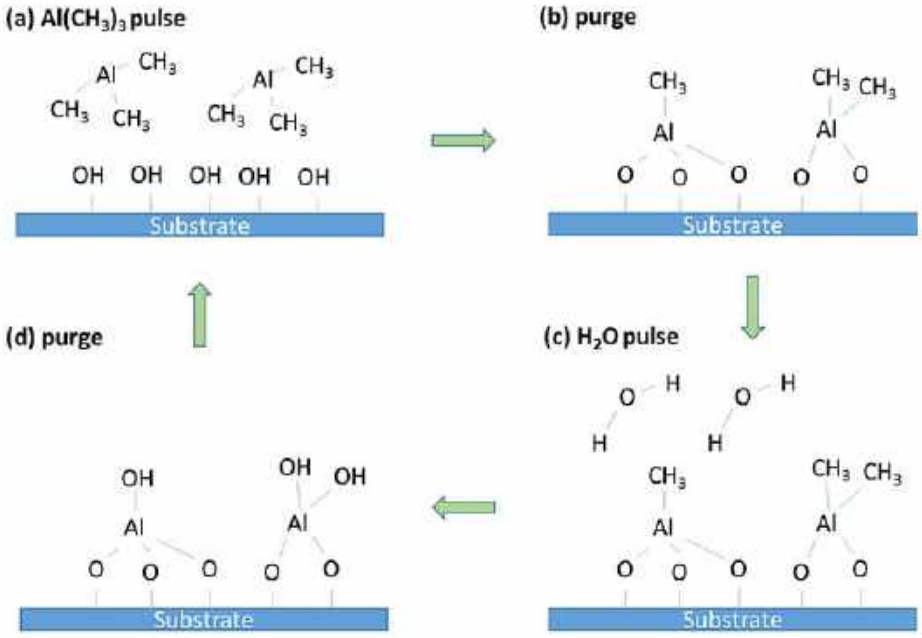

Figure A.3: Cycle of ALD deposition of Al_2O_3. (a) A hydroxylated surface is exposed to a TMA pulse. The Al reacts with the OH group and (b) the remaining TMA and CH_4 is removed via purging. (c) A pulse of water flows through the ALD chamber, replacing the CH_3 groups with OH. (d) A purge follows to empty the chamber of any precursor materials and residues. The cycle is repreated until desired thickness is accomplished. Taken from [43].

A.3 Sputter deposition

Sputter deposition was used as a part of generating a FIB lamella from a sample with AuNPs on Si wafer. It was also used to deposit PtPd on the sapphire samples to avoid charging during SEM imaging.

Sputter deposition is a physical vapour deposition technique of a material onto a substrate through ejection of a material from a sputtering target. It is done through bombardment of particles using a sputtering gas. A schematic image of sputter deposition is seen in figure A.4.

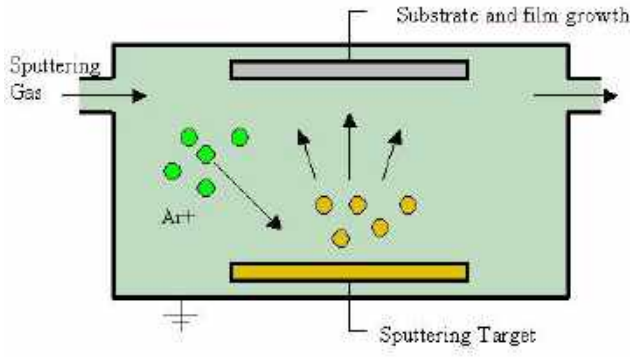

Figure A.4: The workings of sputter deposition. High energy Ar+ ions are bombarding the sputtering target to deposit material onto the substrate surface. Taken from [44]

The particles used as a sputtering gas, such as Ar^+ ions, are generated through an ion source or plasma. The sputtering gas has high energy and when the ions hit the sputtering target material, it results in scattering of the sputtering target material and deposition onto the substrate. So the sample will become covered with a uniform thin film of the desired material [44].

A.4 Focused Ion Beam

With the high resolution of the TEM, the interfacial chemical interaction on atomic level can be studied. However, to examine a sample in TEM requires the samples to be very thin [45, 46]. To create these small TEM friendly samples, a FIB was used on a sample of this thesis to cut out a lamella to study in TEM.

FIB allows controlled manipulation/disruption of a local area on a nanometer scale. Heavy ions, such as Ga^+, are generated by a Liquid Metal Ion Source. The Ga^+ ions are extracted from the source using a strong electric field, and bombard the sample where manipulation/milling is desired. The bombardment of ions leads to atoms being removed from that specific area [45, 46]. Alternating the primary beam currents allows the user to control where milling/manipulation can occur [47].

A FIB and a SEM are often combined, allowing site specific sputtering of atoms on the sample [45]. A schematic of a FIB combined with a SEM is shown in figure A.5

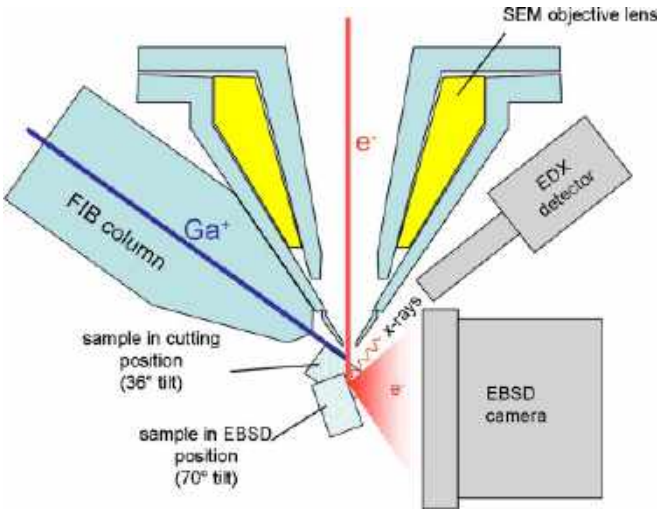

Figure A.5: A FIB combined with a SEM. For cutting, a specific tilt of the sample is required. The sample is surrounded with different detectors. Taken from [46].

B Microscopy methods

B.1 Scanning probe microscopy - Atomic force microscope

SPM includes all techniques where a nanometer sized tip is moved back and forth across a sample to create an image of the surface. SPM can be used in imaging of atoms [48] and NWs [49]. It is not possible to see the surface directly as when using an optical microscope, but a computer generates a topology image from data collected when the tip is moved [48].

One type of SPM is AFM, being the method used in the experiments of this thesis. The AFM tip can manipulate small, unsintered NPs, and can thus be used to move individual particles which are loosely bound to the substrate surface [50].

The AFM operates in three possible modes; contact, non contact and tapping mode. The most used mode in an AFM is the contact mode, with the AFM tip in close contact with the sample surface. The deflection of the cantilever in contact mode AFM is sensed and adds a voltage to the piezo element of the cantilever to raise or lower the tip back to a desired value of deflection. A schematic of contact AFM is shown in figure A.6a [51].

Non-contact mode in AFM is used when there is a possibility that the tip of the AFM might alter the samples in some undesired way. The tip hovers above the sample and van der Waals forces between the tip and the samples are detected and used to create an image of the surface. A schematic of non-contact AFM is shown in figure A.6b [51].

The third mode in AFM is the tapping mode AFM, seen in figure A.6c. This method is used on samples that are easily damaged or otherwise difficult to image as it avoids factors such as friction and adhesion. The tip of the AFM has a small oscillation, which results in the tip alternating between being in contact with the sample surface and not. This mode is sensitive to changes if frequency of the tip, occurring when the tip interacts with an object, such as a NP [51]. With regard to the height measurements in this thesis, tapping mode AFM was used for imaging.

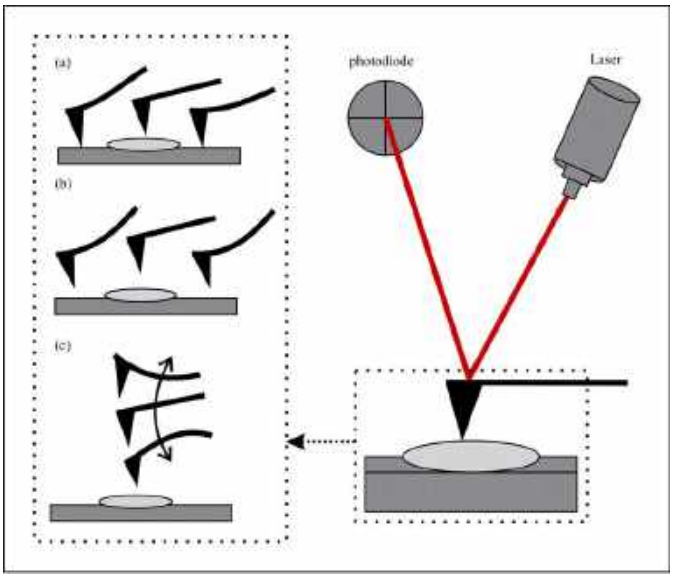

Figure A.6: Schematics of (a) contact mode AFM, (b) non-contact mode AFM and (c) tapping mode AFM. Taken from [52].

B.2 Electron microscope

In this thesis, the electron microscopy techniques SEM and TEM were used for imaging of the samples.

Both SEM and TEM are electron microscopes, which means that the resolution of the created image is not dependent on the wavelength of light, but on the wavelength of electrons. The wavelength of the electrons is much shorter than that of ordinary light and allows resolution on an atomic scale. The resolution, however, is limited by factors such as quality of the electromagnetic lenses used in the microscopes [38] and the interaction volume [53].

In SEM, as the name suggests, the electron beam scans across the surface of the sample and collects electrons that escape from the sample. The electrons scattered from the sample are collected using a set of different detectors placed around the sample holder [54]. A certain tilt as well as rotation can be achieved in SEM and TEM if desired. The samples imaged in SEM can be mounted on different sample holders depending on the type of desired imaging, such as vertically [55].

To image samples in TEM requires the samples to be below 200 nm in thickness for the transmission of electrons to occur and for the scattered electrons to reach the detectors and allow imaging [54].

SEM is a fast, easily operable and a good way to get an overview of samples with a size range of the objects being on the nanometer scale [38]. It can create images being magnified 1-2 million times, which however is low compared to the TEM which can magnify up to 50 million times [54]. Also, the resolution of SEM is approximately 0.4 nm, compared to TEM having the resolution of 0.5 Å [56].

TEM images are 2D projections of the sample studied with a lower depth of field [56] as compared to the SEM images being 3D projections [54]. This can make TEM samples harder to interpret. TEM imaging is more time consuming and more difficult to operate than SEM. [38]

Appendix B

Experimental data

A Particle measurements and development

A.1 AuNPs on Si

The number of particles measured, with regard to the AuNPs situated on Si for Method 1, is described in Table B.1. Some measurements are missing due to unexpected changes occurring between the particle and the substrate, so the contact angles could not be measured.

Table B.1: Presents the number of measured particles using Method 1, for the AuNPs situated on the Si wafer.

	Before sinter	**10 min, 600°C**	**30 min, 600°C**	**3 min, 900°C**
30 nm	60	60	-	-
60 nm	90	89	72	76
90 nm	74	75	98	84

The amounts of particles that were measured on for the AuNPs being situated on Si is shown in Table B.2, when Method 2 was used.

Table B.2: Presents the number of measured particles using Method 2, the height and diameter, for AuNPs situated on the Si wafer.

		Before sintering	**10 min, 600°C**	**30 min, 600°C**	**3 min, 900°C**
30 nm	**Diameter**	76	76	80	93
	Height	24	39	28	20
60 nm	**Diameter**	68	72	60	96
	Height	17	23	19	34
90 nm	**Diameter**	60	56	62	120
	Height	26	20	27	19

The height and width of the AuNPs on a Si wafer after different sintering times and temperatures are shown in Table B.3.

Table B.3: Diameter and height of AuNPs on Si substrate determined by ImageJ and AFM, respectively, after different sintering temperatures and times.

			600°		***900°***
		Before sinter	**10 min**	**30 min**	**3 min**
30 nm NP					
	Diameter (nm)	32.5±0.4	32.1±0.5	31.3±0.1	32.3±0.6
	Height (nm)	28.4±1.8	28.5±2.5	29.5±1.1	26.7±1.7
60 nm NP					
	Diameter (nm)	61.3±1.2	60.7±1.0	59.1±1.1	60.6±0.7
	Height (nm)	55.3±2.1	56.4±2.8	57.5±3.2	54.7±1.8
90 nm NP					
	Diameter (nm)	95.3±5.7	90.0±1.4	91.6±1.6	92.4±1.0
	Height (nm)	84.5±2.4	86.2±4.7	80.7±8.8	90.1±3.5

Representative images of the shape development of 60nm AuNPs on Si substrates are shown in figure B.1.

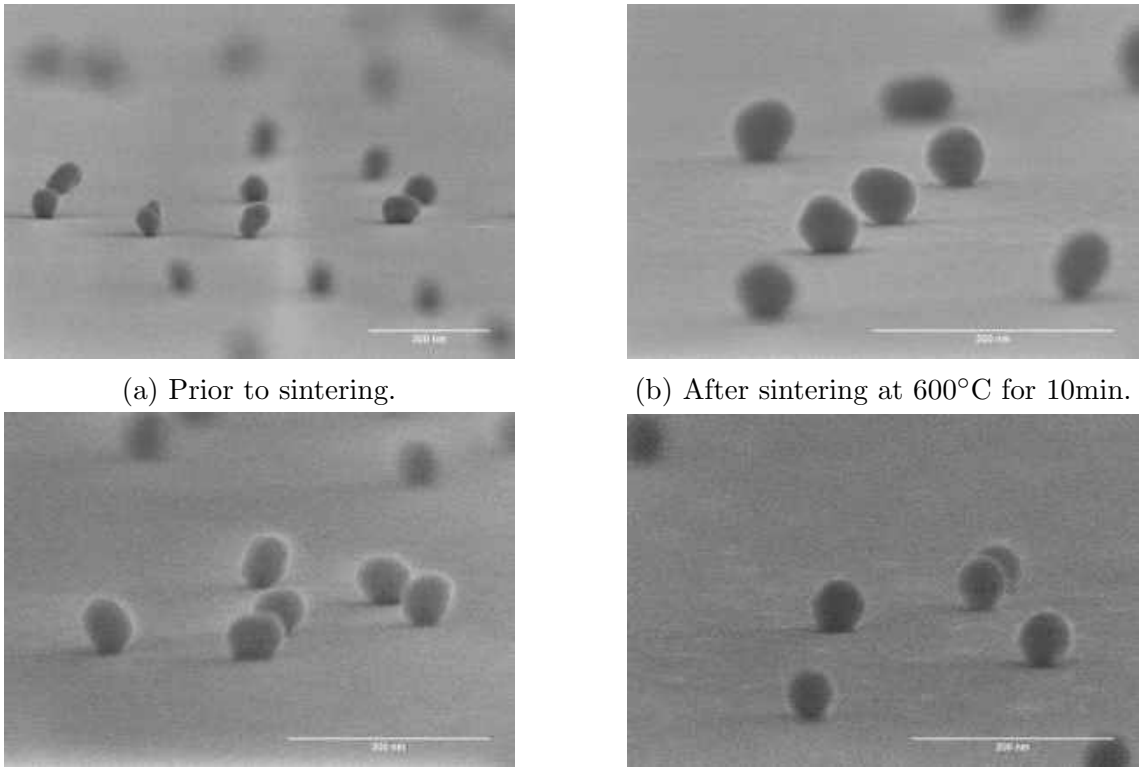

(a) Prior to sintering.

(b) After sintering at 600°C for 10min.

(c) After sintering at 600°C for 30min.

(d) After sintering at 900°C for 3min.

Figure B.1: Changes of 60nm AuNPs sintered at different times and temperatures.

Representative images of the shape development of 90nm AuNPs on Si substrates are shown in figure B.2.

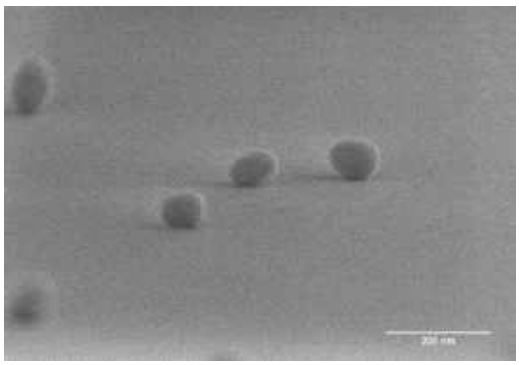

(a) Prior to sintering.

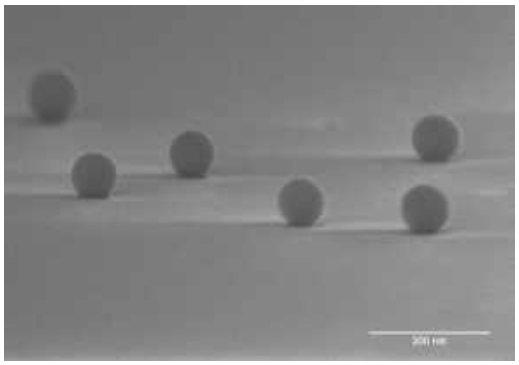

(b) After sintering at 600°C for 10min.

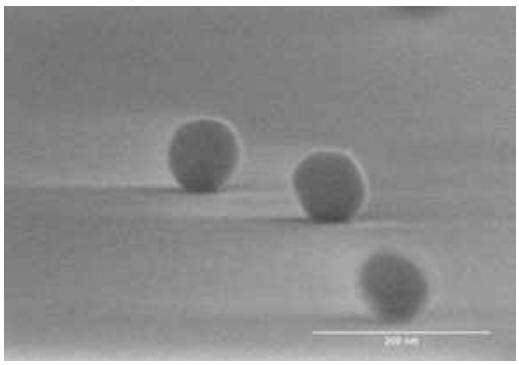

(c) After sintering at 600°C for 30min.

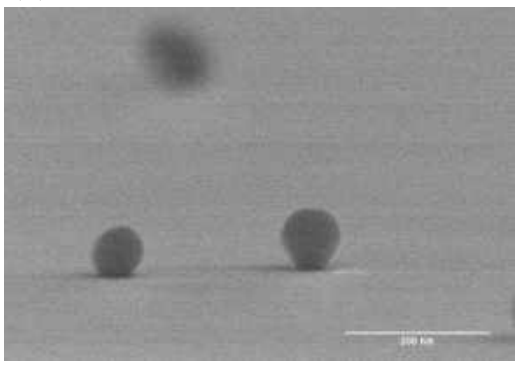

(d) After sintering at 900°C for 3min.

Figure B.2: Changes of 90nm AuNPs sintered at different times and temperatures.

A.2 AuNPs on sapphire

The number of particles that were used for measurements of Method 1 of AuNPs situated on Si, thus contact angle measurements, are presented in Table B.4.

Table B.4: Presents the number of measured particles using Method 1, for the AuNPs situated on the sapphire wafers.

	Before sintering	**After sintering**
30 nm	53	45
60 nm	40	37
90 nm	36	34

The number of AuNPs on Si that were used for measurements of Method 2, thus for height and the diameter measurements, are presented in Table B.5.

Table B.5: Presents the number of measured particles using Method 2, for the AuNPs situated on sapphire wafers.

		Before sintering	**After sintering**
30 nm	**Diameter**	70	68
	Height	24	32
60 nm	**Diameter**	52	64
	Height	17	35
90 nm	**Diameter**	97	74
	Height	26	27

The heights and diameters, extracted using AFM and SEM respectively, after 75 hours of sintering at 800°C of AuNPs situated on sapphire is presented in Table B.6. These values were used for calculating the contact angles using Method 2.

Table B.6: Shows heights and diameters of the differently sized AuNPs situated on sapphire substrates, after sintering at 800°C for 75 hours.

	Diameter (nm)	**Height (nm)**
30 nm	26.3±1.7	23.2±1.4
60 nm	61.1±1.1	52.2±3.3
90 nm	95.0±1.7	79.2±2.5

B Contact angles

The contact angles of 60 nm particles are shown in Figure B.3 after different sintering times. The orange stacks represent the contact angles measured using Method 1 and the yellow stacks represent the contact angles retrieved using Method 2. The error bars indicate the 95% confidence interval.

Since no faceted shape was detected, Method 1 only entails measuring the contact angle ϑ directly.

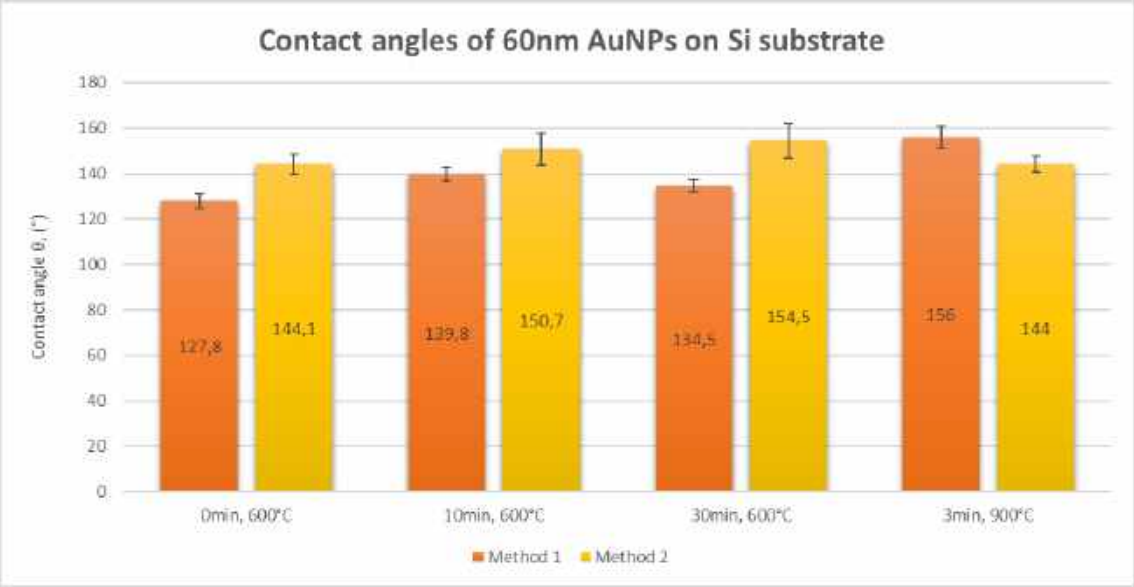

Figure B.3: Contact angles, ϑ, of 60nm AuNPs on Si substrates determined using Method 1 (orange bars) and Method 2 (yellow bars). The error bars indicate the 95% confidence interval.